Paul F. Derwent

E-741

THE UNIVERSITY OF CHICAGO

A MEASUREMENT OF $\sigma(W \rightarrow e\,\nu)$ AND $\sigma(Z^0 \rightarrow e^+e^-)$ IN $\bar{p}p$ COLLISIONS AT $\sqrt{s} = 1800$ GEV

A DISSERTATION SUBMITTED TO
THE FACULTY OF THE DIVISION OF THE PHYSICAL SCIENCES
IN CANDIDACY FOR THE DEGREE OF
DOCTOR OF PHILOSOPHY

DEPARTMENT OF PHYSICS

BY
PAUL F. DERWENT

CHICAGO, ILLINOIS
DECEMBER, 1990

Acknowledgements

In my four year path to graduation, I have had the pleasure of working with many people. I have learned from them, been confused with them, stayed up late with them, and drank beer with them. This section will attempt to remember everyone who has help me in the steps along the path.

I wish to thank Henry, who served as my advisor and friend through graduate school. He got me started in experimental physics with monopoles and persuaded me to move on to higher energies and bigger detectors.

I wish to thank Dan, Tony, and Jay, who were here when I started. They helped get me involved in the trigger and understand how it worked. They got me started on the wonderful projects of charge injection, LUMMON, and trigger table parsing, in which I learned lots of how things work at B0. In addition, they gave good advice and instruction on how to advance as a graduate student.

I wish to thank Sunil, George, Rick, and Tsai, my office mates for two years (and more) for discussions, insights, and general good times. They helped me fit in as a graduate student and were always willing to take the time to answer my questions.

I wish to thank Aaron, Tim, Roy, Lawrence, Ritchie, Hans, John, and the rest of my fellow graduate students in HEP who were always willing to turn away from the terminal and talk about anything. They have made the days much more enjoyable.

I wish to thank Mel, Carla, and Myron, who oversaw my development as a graduate student and always gave good suggestions and projects to work on. Without them, I would not know the intricacies of the cluster bus or the CDFDB.

I wish to thank Steve, Keith, Dee, Geri, Jim, Brian, Dave, Liz, JJ, and the B0 staff, who taught me all that I know (and sometimes more than I wanted to know) about RABBIT, FASTBUS, the Resource Manager, Run_Control, the data acquisition system, and the production manager, as well as where to find what I needed in the many unknown places around B0.

I wish to thank my fellow CDF graduate students, especially Aaron, Brian, Les, Vic, Phil, William, Peter, Leigh, Jodi, Karen, Tim, and Tim, with whom I spent many days (and nights) at B0 and doing analysis. I must admit that it would have been impossible to reach this stage without them.

I wish to thank Claudio and Marshall, with whom this work was done. They have taught me much about how to do physics and how to survive as a student. It would have taken me three time as long (or more) to do this work without them.

I wish to thank the University of Chicago Physics department, specifically the High Energy Physics group for providing me with the opportunity to study physics. They accepted me, taught me, supported me, sent me to Europe, gave me advice, and graduated me.

I wish to thank Dave and Adam, my roommates for three years in Chicago. We have drunk a lot of Campari and spent a lot of time together – I would not trade these opportunities and discussions for anything.

I wish to thank Sam and Hobbes, residents of my apartment along with Dave

and Adam. They never cared whether you had finished projects in time, as long as I remembered to feed them in the morning and scratch behind their ears.

I wish to thank my sister Margaret, who integrated me into Chicago and the world of Booth-Hansen. She gave me plenty of opportunities to wear a tie and to spend time with a different set of people.

I wish to thank my parents, who have supported me throughout my graduate career. Even when I have been most confused, they let me know that I could count on them for help whenever and however it was needed.

I wish to thank Lou Holtz and the rest of the Fighting Irish, who made it possible for me to enjoy Saturday afternoons again. I am especially grateful for the 1988 championship season.

I wish to thank all my friends who have thought enough of me to call, write, invite me to their weddings, and generally be friends. Life would be a drag without the support of friends.

Thanks to all of you.

Table of Contents

List of Tables

List of Illustrations

Abstract

An analysis of high transverse momentum electrons using data from the Collider Detector at Fermilab in $\bar{p}p$ collisions at $\sqrt{s} = 1800$ GeV yields values of the production cross section times branching ratio for W and Z^0 bosons of $\sigma(W \rightarrow e\,\nu) = 2.19 \pm 0.04$ (stat) $\pm$ 0.21 (sys) nb and $\sigma(Z^0 \rightarrow e^+e^-) = 0.209 \pm 0.013$ (stat) $\pm$ 0.017 (sys) nb. Detailed descriptions of the CDF electron identification, background, efficiency, and acceptance are included. Theoretical predictions of the cross sections that include a mass for the top quark larger than the W mass, current values of the W and Z^0 masses, and higher order QCD corrections are now in good agreement with these measured values.

Chapter 1

Introduction

It was Oscar Klein in 1938 who first proposed a W boson as the mediator of the weak interaction [1, 2] as a modification of Fermi's four point interaction [3] by the addition of a massive charged vector boson. These theories were formulated in analogy with the emission of a photon in electromagnetic transitions to explain nuclear β–decay, the emission of an electron and a neutrino in the decay of a neutron. The W boson was taken to have charge $\pm$ 1, since nuclear β–decay is charge changing, and be rather massive, since the weak interaction has such a short range.

In the next twenty years, there was much progress in the understanding of the weak interaction, but very little concerning the weak boson. The $V - A$ form of the weak interaction led to definite predictions involving neutrino scattering which diverged as the center of mass energy grew [2]. Since the presence of a vector boson to mediate the weak interaction solves this divergence problem, interest in the W rose again.

With the understanding of electromagnetism in terms of a quantum field theory [4] and the work of Yang and Mills to apply field theoretic concepts to non-Abelian gauge fields [5], Schwinger attempted to unify the electromagnetic and weak interactions in terms of a gauged field theory [6]. The weak boson in his theory did acquire a mass through couplings to auxiliary scalar and pseudoscalar fields. The

magnitude of the boson mass was not predicted. Schwinger's model encountered problems as it did not account for the $V - A$ form of the weak interaction.

Following the work in understanding symmetry breaking by Nambu [7], Goldstone [8], and Higgs [9], the Glashow-Weinberg-Salam model [10] incorporated the idea of a massive W boson in a unified gauge theory which gave masses to the vector bosons (and kept the photon massless) while preserving the gauge invariance of the Lagrangian. This model gives predictions for the masses and coupling of the W and Z^0 bosons.

With predictions for the masses and couplings, the production and decay properties of W and Z^0 bosons in $\bar{p}p$ collisions can be predicted. It is necessary to also take into account the parton momentum distributions and QCD corrections in calculations of the production cross sections for the W and Z^0. This paper presents a measurement of the production and subsequent decay into electrons of W and Z^0 bosons in $\sqrt{s} = 1800$ GeV $\bar{p}p$ collisions at the Collider Detector at Fermilab (CDF).

In comparing the experimentally measured production cross sections to theoretical predictions, all aspects of the model are tested simultaneously. The boson couplings to fermions, the masses of the bosons, the parton momentum distributions, and the QCD color factors and corrections all play a part in the theoretical prediction of the cross sections. The understanding of all of these quantities has improved significantly in the last decade, improving the precision of the predicted cross sections. The ability to do the experiments has also increased significantly in the last decade (the W and Z^0 were first seen just 7 years ago [11]), improving the precision of the measured cross sections. The precision of both theoretical predictions and experimental measurements is now at the stage where each tests the other's abilities.

1.1 Brief History of W and Z^0 Cross Section Measurements

Experimental searches for the charged vector boson which served as the mediator of the weak interaction began during the 1960's. Experiments placed limits on the cross section and subsequent decay into muons for W's in the mass range of a few GeV/c^2 [12]. The proof (by 't Hooft [13] in 1971) of the renormalization of spontaneously broken gauge theories led to general interest in the Glashow-Weinberg-Salam model of electroweak interactions. This model proposed a much different mass range for the weak charged and neutral vector bosons. Experiments with neutrino beams which had seen evidence for charged current interactions then began to look for evidence of neutral current interactions. The discovery of neutral current interactions [14] in 1973 was a great triumph for the electroweak model.

Following on this indirect evidence for the W and Z^0 bosons, high energy hadron-hadron colliders were proposed to find direct evidence of the W and Z^0 [15]. The S$\bar{p}p$S at CERN with a center of mass energy $\sqrt{s}$ = 546 GeV was the first of these machines.

Using 4π detectors and looking for the signal of both leptons in the decay of the W or Z^0, the UA1 and UA2 experiments at CERN saw direct evidence of W and Z^0 production [11] in 1983. In subsequent years, with a higher center of mass energy $\sqrt{s}$= 630 GeV, these collaborations accumulated large datasets of W and Z^0 events, identifying them in their decays to electrons, muons, taus, and hadrons [16].

In 1985, the Tevatron at FNAL began operation in the colliding beam mode with a center of mass energy $\sqrt{s}$ = 1800 GeV. CDF first saw the W and Z^0 during the 1987 run [17] with an integrated luminosity of approximately 26 nb^{-1}. In the data run of 1988-89, CDF recorded an integrated luminosity of approximately 4.0 pb^{-1}. This paper reports on results of measurements of the cross section times branching ratio for W and Z^0 production using this high statistics dataset.

CDF has previously published [18] a measurement of the ratio of $\sigma(W \rightarrow e\,\nu)$ to $\sigma(Z^0 \rightarrow e^+e^-)$ in $\bar{p}p$ collisions at $\sqrt{s} = 1800$ GeV. From this measurement, the total width of the W boson was extracted. The measurements of the individual cross sections are related to the measurement of the ratio — given two of these three quantities, the third is easily extracted. In the analysis of the ratio of the cross sections, we applied selection criteria to minimize the systematic error in the ratio. In order to lower backgrounds and minimize systematic uncertainties, events with energy clusters other than the electrons from W and Z^0 decays were rejected in this analysis. Such a requirement is fine in measuring the cross section ratio, where both numerator and denominator are affected equally, but not for the independent measurements of the numerator and denominator. This paper describes the independent measurements of the W and Z^0 cross sections, while the analysis cited in reference [18] contains our best understanding of the ratio of cross sections and the W width.

1.2 Underlying Physics Process

W and Z^0 bosons are produced in $\bar{p}p$ collisions through the Drell–Yan process [19], the annihilation of a quark and an anti-quark into a boson. The subprocess cross section can be directly calculated in the context of the Standard Model [20] with knowledge of the quark couplings to the boson and the boson mass.

To go from the subprocess cross section to the $\bar{p}p$ cross section requires knowledge of the quark (and gluon) momentum distribution functions inside the protons. These functions are found by fitting data from μ, e, and ν inelastic scattering data. These functions must be evolved to the Q^2 scale of W and Z^0 production from lower energy regimes where the inelastic scattering data has been taken [21].

The lowest order Drell–Yan process does not take into account QCD corrections due to QCD processes such as gluon radiation from the incoming quarks. These

processes are expected to increase the total cross section by roughly 30% [22]. With the inclusion of this K factor, the total production cross section of W and Z^0 bosons in $\bar{p}p$ collisions can be predicted.

Given a total production cross section, the branching fraction of the bosons to electrons is still needed. The partial widths into electrons can be calculated with knowledge of the lepton couplings, but more information is necessary for the calculation of the full width. The full width depends upon the total number of possible decay channels for the bosons. With this information, the branching fraction can be calculated.

1.3 Outline of Paper

This paper describes the identification of W and Z^0 bosons through their decay into electrons and therefore concentrates on the identification and selection of electrons in the CDF detector. High transverse momentum electrons leave distinctive and easily recognizable signatures and, because of their large mass, the W and Z^0 bosons serve as the dominant source of these electrons.

Section 2 describes the relevant systems of the detector in the identification of electrons. Section 3 describes the trigger requirements for electrons. Section 4 contains descriptions of the analysis and the datasets used in the measurement of $\sigma(W \rightarrow e\,\nu)$ and $\sigma(Z^0 \rightarrow e^+e^-)$ in $\bar{p}p$ collisions at $\sqrt{s} = 1800$ GeV. The discussions of the electron kinematical and geometrical acceptance (section 5), background subtraction (section 7), and electron selection efficiency (section 6) follow. Further corrections and the calculation of the integrated luminosity are detailed in sections 8 and 9. The paper closes with a discussion of $\sigma(W \rightarrow e\,\nu)$ and $\sigma(Z^0 \rightarrow e^+e^-)$ in $\bar{p}p$ collisions at $\sqrt{s} = 1800$ GeV and a comparison to theoretical predictions.

Chapter 2

Detector Description

The CDF detector is an azimuthally and forward–backward symmetric detector designed to study the physics of $\bar{p}p$ collisions at the Fermi National Accelerator Laboratory (FNAL) Tevatron. Event analysis is based on charged particle tracking, magnetic momentum analysis, and fine grained calorimeters. CDF attempts to measure the energy, momentum, and, in a limited number of cases, the identity of particles produced at the Tevatron collider over a large fraction of the solid angle. Particles produced in $\bar{p}p$ interactions pass through a thin Be beam pipe, charged particle tracking chambers, sampling calorimeters, and muon chambers. Figure 1 shows a side view of the CDF detector.

It is beyond the scope of this paper to describe in detail all aspects of the CDF detector. Such a description can be found in reference [23]. We will concentrate on the pertinent aspects for the analysis and detection of $W \rightarrow e\ \nu$ and $Z^0 \rightarrow e^+e^-$ events, specifically those concerning energy and momentum measurement.

2.1 Calorimeters

The CDF calorimeter covers the range from 2° to 178° in polar angle and 2π in azimuth, segmented into projective towers in azimuth and pseudorapidity [24]. The

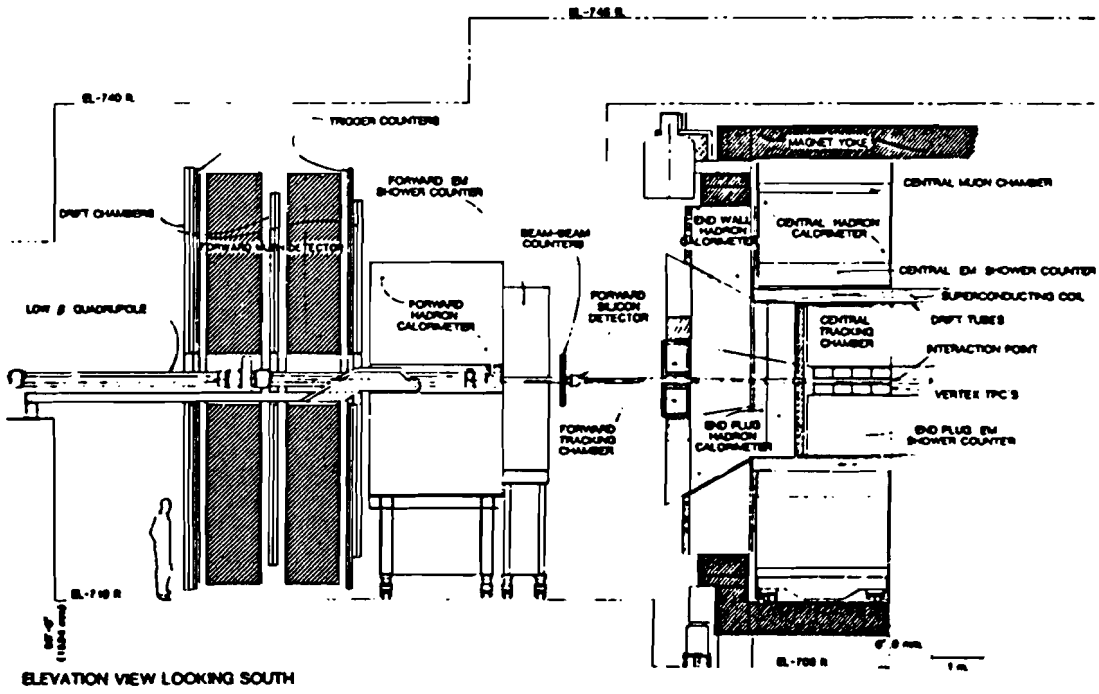

ELEVATION VIEW LOOKING SOUTH

Figure 1. A side view of one half of the CDF detector. It is symmetric about the $\eta = 0$ plane.

coverage consists of three separate regions, called the central, plug, and forward regions. The central region covers the range $|\eta| < 1.1$, the plug region covers $1.1 < |\eta| < 2.4$, and the forward region covers $2.2 < |\eta| < 4.2$. Each region consists of combined electromagnetic and hadronic calorimeters. The calorimeter systems are summarized in table 1. A description of the accepted fiducial regions of the calorimeter coverage is found in section 5.1.

2.1.1 The Central Calorimeter

The calorimeters in the central region use scintillator as the active medium with phototube readout. Figure 2 shows a perspective view of a central calorimeter wedge, which covers $0 < \eta < 1.1$ and 15° in ϕ. The electromagnetic compartment (CEM) [25] uses lead sheets interspersed with polystyrene scintillator and is 18 radiation lengths and 1 absorption length thick. The tower size is ~ 0.1 in η and 15° in ϕ. The CEM has an energy resolution of $\frac{13.5\%}{\sqrt{E}} + 1.7\%$ [26]. Located approximately 6 radiation lengths into the compartment (shower maximum for electromagnetic showers) is a proportional chamber (strip/wire chamber), which gives shower position measurements in both the Z and $R\phi$ views. This chamber has a position resolution of 0.2 cm by 0.2 cm. The calorimeter is physically segmented into 15° sections in azimuth and along the $\eta = 0$ plane in Z.

The hadronic compartment (CHA) [27] uses steel plates interspersed with acrylic scintillator and is 4.5 absorption lengths thick. The tower size is ~ 0.1 in η and 15° in ϕ. The CHA has an energy resolution measured to be $\frac{80\%}{\sqrt{E}} + 3\%$ for isolated pions [28].

2.1.2 The Plug Calorimeter

The calorimeters in the plug region use gas proportional chambers with cathode pad readout. Figure 3 shows a perspective view of a plug calorimeter quadrant. The

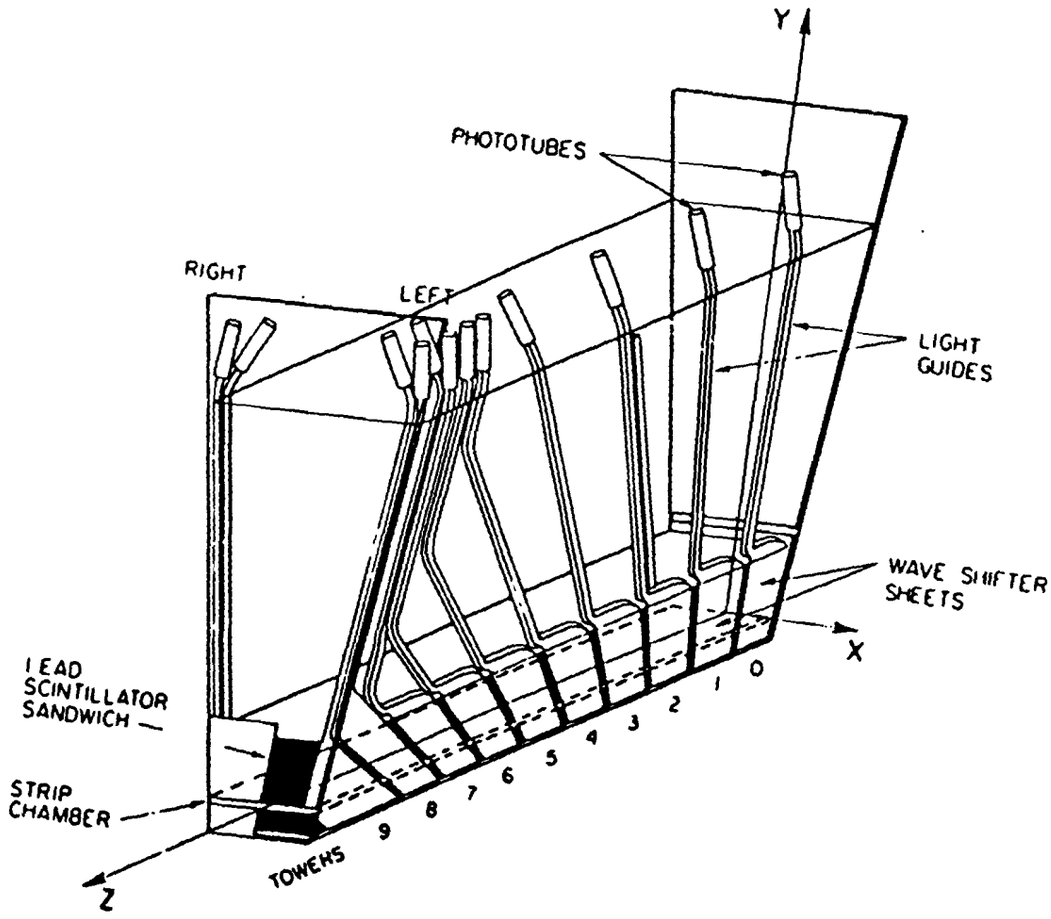

Figure 2. A perspective view of a central calorimeter wedge.

electromagnetic compartment (PEM) [29] uses lead absorber panels interspersed with conductive plastic proportional tube arrays, and is 18-21 radiation lengths and 1 absorption length thick. The tower size is 0.09 in η and 5° in ϕ. The PEM has an energy resolution estimated to be $\frac{28\%}{\sqrt{E}} + 2.0\%$. The shower position is measured using the information from the θ and ϕ strips and has a resolution of 0.2 cm × 0.2 cm. The calorimeter is divided into quadrants.

The hadronic compartment (PHA) [30] uses steel plates interspersed with conductive plastic proportional tube arrays and is 5.7 absorption lengths thick. The tower size is 0.09 in η and 5° in ϕ. The PHA has an energy resolution estimated to be $\frac{130\%}{\sqrt{E}} + 4\%$ for isolated pions.

2.1.3 The Forward Calorimeter

The calorimeters in the forward region also use gas proportional chambers with cathode pad readout. Figure 4 shows a perspective view of a forward calorimeter quadrant. The electromagnetic compartment (FEM) [31] uses lead absorber panels interspersed with conductive plastic proportional tube arrays, and is 25.5 radiation lengths and 1 absorption length thick. The tower size is 0.1 in η and 5° in ϕ. The FEM has an energy resolution estimated to be $\frac{25\%}{\sqrt{E}} + 2.0\%$ and is linear up to 160 GeV. The shower position is measured using the information from the θ and ϕ strips and has a resolution of 0.1 cm to 0.4 cm depending upon the location in the calorimeter.

The hadronic compartment (FHA) [32] uses steel plates interspersed with conductive plastic proportional tube arrays and is 7.7 absorption lengths thick. The tower size is 0.1 in η and 5° in ϕ. The FHA has an energy resolution estimated to be $\frac{130\%}{\sqrt{E}} + 4.0\%$ for isolated pions.

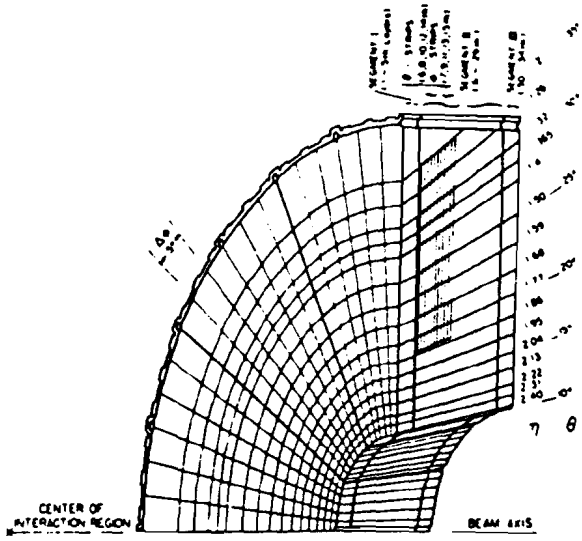

Figure 3. A perspective view of a plug calorimeter quadrant.

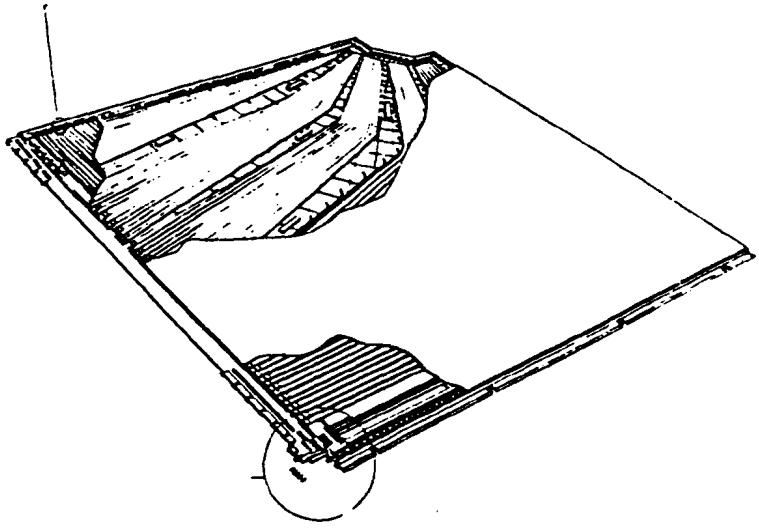

Figure 4. A perspective view of a forward calorimeter quadrant.

Table 1. Summary of CDF calorimeter properties

System	η Range	Energy Resolution ($\frac{\%}{\sqrt{E}}$) + constant term	Position Resolution	Thickness
CEM	$\|\eta\| < 1.1$	13.5% $\oplus$ 1.7% (constant)	0.2 cm $\times$ 0.2 cm	18 X_0
PEM	$1.1 < \|\eta\| < 2.4$	28% $\oplus$ 2% (constant)	0.2 cm $\times$ 0.2 cm	18-21 X_0
FEM	$2.2 < \|\eta\| < 4.2$	25% $\oplus$ 2% (constant)	0.1 cm to 0.4 cm	25 X_0
CHA	$\|\eta\| < 1.1$	80% $\oplus$ 3% (constant)	0.2 cm $\times$ 0.2 cm	4.5 Λ_{abs}
PHA	$1.1 < \|\eta\| < 2.4$	130% $\oplus$ 4% (constant)	0.2 cm $\times$ 0.2 cm	5.7 Λ_{abs}
FHA	$2.2 < \|\eta\| < 4.2$	130% $\oplus$ 4% (constant)	0.2 cm $\times$ 0.2 cm	7.7 Λ_{abs}

2.2 Tracking

The CDF tracking system covers the angular range $\sim$ 8° to $\sim$ 172° in polar angle and is contained within a 1.412 T axial magnetic field. Three dimensional track reconstruction is available in the range 40° to 140°. The tracking system consists of two separate detectors, one used to measure charged track position over a large angular range and the second to measure charged particle momenta and position. The tracking systems are summarized in table 2.

2.2.1 Vertex Time Projection Chambers

Immediately outside the beam pipe, eight small vertex time projection chambers (VTPC) [33] measure charged particle positions over the angular range $\sim$ 8° to $\sim$ 172°. The VTPC system is 2.8 m long, which offers good coverage of the long interaction region at the Tevatron (the rms of the vertex Z distribution is 30 cm). Sense wires give measurements of track coordinates in RZ and pads are used to measure in $R\phi$. Reconstructed track segments in the VTPC are used to measure

Table 2. Properties of the CDF tracking chambers

Tracking System	Angular Coverage	2 Track Resolution	Momentum Resolution (δp_T / p_T)
VTPC	$\sim 8° < \theta < \sim 172°$	6 mm/θ (Z) 6 mm (R) 3 cm (ϕ)	-
CTC	$40° < \theta < 140°$	3.5 mm	0.0011 × p_T (GeV/c)

the location of the interaction vertex position, Z_{vert}, with a resolution of 1 mm in the Z direction.

2.2.2 Central Tracking Chamber

The Central Tracking Chamber (CTC) [34] is a 1.3 m radius 3.2 m long cylindrical drift chamber which gives precise momentum determination and spatial position in the range 40° to 140° ($|\eta| < 1.0$). The chamber consists of 84 layers of sense wires, grouped into alternating axial and stereo superlayers. The axial layers consist of 12 sense wires, the stereo layers have 6 sense wires (tilted at ± 3° relative to the beam direction). The superlayers are tilted at 45° with respect to the radial direction to correct for the Lorentz angle of the electron drift in the magnetic field. Figure 5 shows a cutaway view of the CTC and the wire positions.

The momentum resolution of the CTC is $\frac{\delta p_T}{p_T} = 0.002 \times p_T$ for isolated tracks. With the constraint that the track originates at the interaction vertex, the resolution improves to $\frac{\delta p_T}{p_T} = 0.0011 \times p_T$ by extending the effective tracking radius from 1 m to 1.3 m [35].

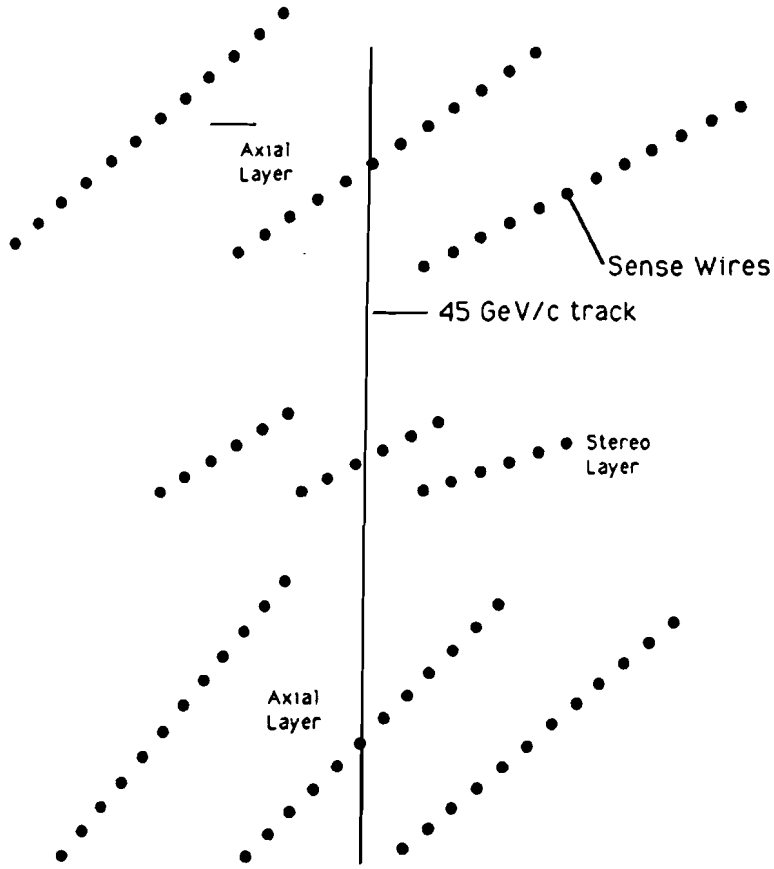

Figure 5. A cutaway view of the CTC. The sense wires are ganged into axial and stereo superlayers, tilted at 45° with respect to the radial direction. Superimposed is the path of a 45 GeV/c p_T track through the chamber.

2.3 Luminosity Monitors

CDF uses scintillator planes located 5.8 m from the nominal interaction point as luminosity monitors. Known as the beam-beam counters (BBCs), these counters cover the angular range 0.32° to 4.47° ($3.24 < |\eta| < 5.90$). They have excellent timing properties ($\sigma < 200$ ps) and provide the best measurement of the time of the interaction. Coincident hits in the BBCs are used to signal an inelastic collision for the trigger system.

Chapter 3

Triggering

The operating environment at a hadron collider requires a very sophisticated trigger system to pick out the physics of interest. The detected inelastic cross section at $\sqrt{s}$ = 1800 GeV is on the order of 50 mb, while the physics of this paper has a production cross section in the range of 2 nb. CDF has designed a 4 level trigger system in order to provide the necessary rejection power [36]. Here we will discuss the triggers used in this analysis.

The levels of the trigger increase in complexity as one goes from Level 0 to Level 3, as each one has more time and more data available in the decision making process. Levels 0, 1, and 2 consist of programmable hardware and use only a subset of the data available for the decision. Level 3 consists of a farm of ACP computers [37] running FORTRAN-77 filter algorithms and has the full detector data available.

The hardware trigger system is designed around the projective nature of the calorimeter towers. Trigger towers have a width of 0.2 in pseudorapidity and 15° in azimuth, mapping the detector into an array of 42 (in η) by 24 (in ϕ) in both electromagnetic and hadronic compartments. A fast two dimensional track finder (CFT) is also an essential part of the trigger hardware [38].

3.1 Level 0

Level 0 is used to signal an inelastic event and consists of a simple coincidence of hits in both east and west BBCs. These hits are required to be within a 15 nsec gate centered on the expected beam crossing. The Level 0 decision is made within the 3.5 μsec between beam crossings, so that no deadtime is incurred when Level 0 does not accept an event.

3.2 Level 1

The Level 1 electron trigger makes use of the calorimeter information only. The electron trigger requires that one trigger tower in the central electromagnetic calorimeter be above a 6 GeV threshold in transverse energy (E_T), which is defined by the polar angle between the vertex position (assumed to be 0 for the trigger) and the calorimeter tower. The Level 1 decision is made within 7 μsec, thus missing the next beam crossing for each event accepted by Level 0 (which at a instantaneous luminosity of 10^{30} /cm^2/sec is about 15% of the time).

3.3 Level 2

The Level 2 electron trigger makes use of both calorimeter and tracking information. A hardware cluster finder searches the electromagnetic tower array to form clusters. The clusters are formed around seed towers, which are required to have at least 4 GeV of transverse energy (E_T), assuming the vertex position to be at $Z = 0$. The 4 nearest neighbors of each seed tower (along the η and ϕ directions) are then searched and included in the cluster if they have $E_T > 3.6$ GeV. Again, the 4 nearest neighbor towers of each tower in the cluster are searched and included in the cluster if they have $E_T > 3.6$ GeV. This algorithm repeats until the cluster can no longer be extended. The hadronic E_T in towers included in the cluster is

added to the electromagnetic E_T to give a total cluster E_T. These clusters are then matched in azimuth with stiff tracks from the CFT.

The Level 2 electron trigger then requires that the cluster have more than 12 GeV in electromagnetic E_T (EM E_T), that the ratio of the total E_T to EM E_T be less than 1.125, and that there be a track associated with the cluster with transverse momentum (p_T) greater than 6 GeV/c. The energy threshold was set to meet two needs:

1. We wished to be highly efficient for W and Z^0 events, as well as the possiblity of semi-leptonic decays of the top quark, which means a low energy threshold.

2. We also wished to have the smallest deadtime due to readout of the detector, which means a high energy threshold.

The balancing of these competitive desires led to the 12 GeV E_T threshold. The requirements on total cluster E_T to EM E_T and the track p_T threshold were set with the same requirements in mind.

3.4 Level 3

Level 3 also uses both calorimeter and tracking information in its decision. As the full detector data is available to the Level 3 processors, fast 2-dimensional tracking and the offline clustering algorithms are used. The fast 2-dimensional tracking uses a segment finding and linking algorithm for the axial layers of the CTC. It has an adjustable cutoff in transverse momentum from 900 MeV/c to $\sim$ 20 GeV/c and a resolution of $\delta p_T/p_T = 0.0077 \times p_T$. The offline clustering makes use of the fine segmentation of the calorimeter, using towers with width 0.1 in η and 15° in azimuth for the central region of the calorimeter (see section 4 for more information on this algorithm). The ratio of hadronic E_T to electromagnetic E_T is required to be less than 0.125 to create a cluster.

Event selection in Level 3 requires that (1) there be a cluster with EM $E_T > 12$ GeV and the lateral energy sharing be consistent with that expected from electrons, or (2) there be a cluster with EM $E_T > 20$ GeV. In addition, a track with $p_T > 6$ GeV/c is required, but there is no matching between the track and cluster positions.

Chapter 4

Event Selection

This analysis concentrates on the selection of a isolated, well–measured, high–transverse–momentum electron in the central rapidity region. In this region of the detector, we have available many variables to classify events as having electron candidates. We therefore require the presence of a well identified electron in this region for both W and Z^0 candidate events.

For Z^0 candidates, we also require the presence of a second electron candidate. Given one well identified electron in the central region, we can use loose selection requirements in the identification of a second electron. We therefore accept second electron candidates in a much larger rapidity region.

This section covers the identification of electrons in the CDF. We define the variables used in the selection first. Since the different calorimeter elements have different strengths, the requirements and variables for the central, plug, and forward regions are different. After the definition of the variables, the actual selection requirements for the central electron sample are described. Distributions for the electron variables are shown for the W and Z^0 candidate events. After the explanation of the central electron sample, the separate requirements for the W sample and Z^0 sample are described.

4.1 Electron Identification

4.1.1 Offline Clustering

The CDF electron identification algorithms begin with the formation of electromagnetic clusters. Towers with transverse electromagnetic energy (EM E_T) > 3.0 GeV are used as an array of seeds for clusters. Neighboring towers (daughters) are included in the cluster if they have EM E_T > 0.1 GeV and if the ratio of the daughter tower E_T to the seed tower E_T is less than 1.0. For clustering purposes, E_T is defined by the energy measured in the calorimeter and the polar angle given by the tower center position in the detector and the event vertex. Towers are added to the cluster until the maximum cluster size is reached. This cluster size varies with calorimeter [39]. The maximum cluster size is limited to 3 towers in pseudorapidity ($\Delta\eta \approx 0.3$) by 1 tower in azimuth ($\Delta\phi = 15°$) in the central region, to 5 towers in pseudorapidity ($\Delta\eta \approx 0.5$) by 5 towers in azimuth ($\Delta\phi = 25°$) in the plug region, and 7 towers in pseudorapidity ($\Delta\eta \approx 0.6$) by 7 towers in azimuth ($\Delta\phi = 35°$) in the forward region. The variation in size for the different calorimeters takes into account the fact that the physical tower size changes while the physical shower size stays roughly the same.

4.1.2 Electron Candidates

We require that the EM E_T of the cluster be > 5.0 GeV. In addition, the E_T of the corresponding towers in the hadronic calorimeters is summed. The ratio of hadronic E_T to electromagnetic E_T (Had/Em) must be less than 0.125 for the cluster to be considered as an electron candidate.

4.1.3 Isolation

For every cluster passing these cuts, the variable *Iso* is defined. This variable gives a representation of the presence of other energetic particles near the electron candidate by quantifying the amount of energy in the calorimeter centered in a cone around the electron cluster. The electron isolation is defined as:

$$Iso = \frac{E_T^{cone} - E_T^{cluster}}{E_T^{cluster}} \tag{4.1}$$

where E_T^{cone} is the transverse energy in a cone centered on the electron cluster and includes all towers within a radius, R, equal to $\sqrt{\Delta\eta^2 + \Delta\phi^2}$, where ϕ is measured in radians. In this analysis, the cone radius equals 0.4.

4.2 Region Dependent Variables

We apply additional criteria for electron identification which depend on the calorimeter region in which the cluster is located. Since we require a well identified central electron for both the W and the Z^0 analyses, we use the most stringent requirements in this region. For the plug and forward regions, which are searched for electrons only after finding a well identified central electron, we apply looser requirements. We will first describe the criteria for the central region. The actual values for these requirements will be described later.

4.3 Central Electron Variables

Both the central electromagnetic calorimeter and the CTC cover the range $|\eta| < 1.1$. We require that there be a three dimensional track (in which all three components of momentum are reconstructed) associated with the calorimeter cluster. We use the direction of this track, as measured at the beam line, to define the

electron direction. Using the corrected calorimeter energy (defined in the following section), and the track direction, we define the central electron E_T [40]. In addition, we use the ratio of the corrected calorimeter energy to the track momentum (E/p) to identify electrons.

4.3.1 Electron Response Corrections

The measured energy in the calorimeter is corrected for several known effects. Using the strip cluster position (described below), we correct for the response of a tower as function of the azimuthal and Z position of the shower. This correction has been taken from electron testbeam data [41]. Figure 6 shows the relative response map as a function of shower position for a typical tower in the CEM (the tower calibration used electrons showering in the center of the tower). The accuracy of this response map correction is known to be 1.1% over the the CEM fiducial region (see section 5.1).

We then use a sample of $\sim$ 17,000 electrons with $E_T > 12$ GeV to normalize the calorimeter response. The distributions of measured calorimeter energy to track momentum set a relative response scale for each of the 478 central calorimeter towers. The overall scale is set using a sample of W electrons and the momentum scale of the tracking chamber, which is determined from geometry and the magnetic field. The uncertainty in the tracking chamber scale comes from an investigation of the invariant mass distributions of $J/\Psi \rightarrow \mu^+\mu^-$ and $\Upsilon \rightarrow \mu^+\mu^-$. The E/p distribution for the W sample has been compared to that of a radiative W Monte Carlo [42] that includes both internal and external bremstrahlung. The comparison of the E/p distributions has been used to set the absolute scale of the calorimeter [43]. See figure 7 for the comparison of data and Monte Carlo.

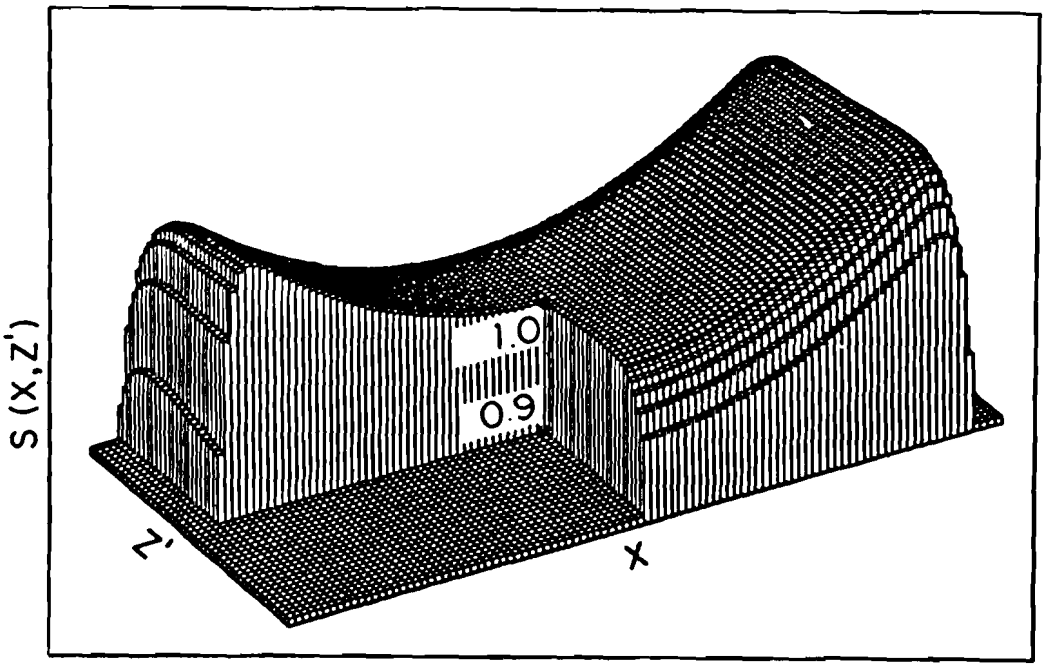

Figure 6. Relative response to electrons in a central calorimeter tower. The Z' axis is in the beam direction and the X axis is in the azimuthal direction.

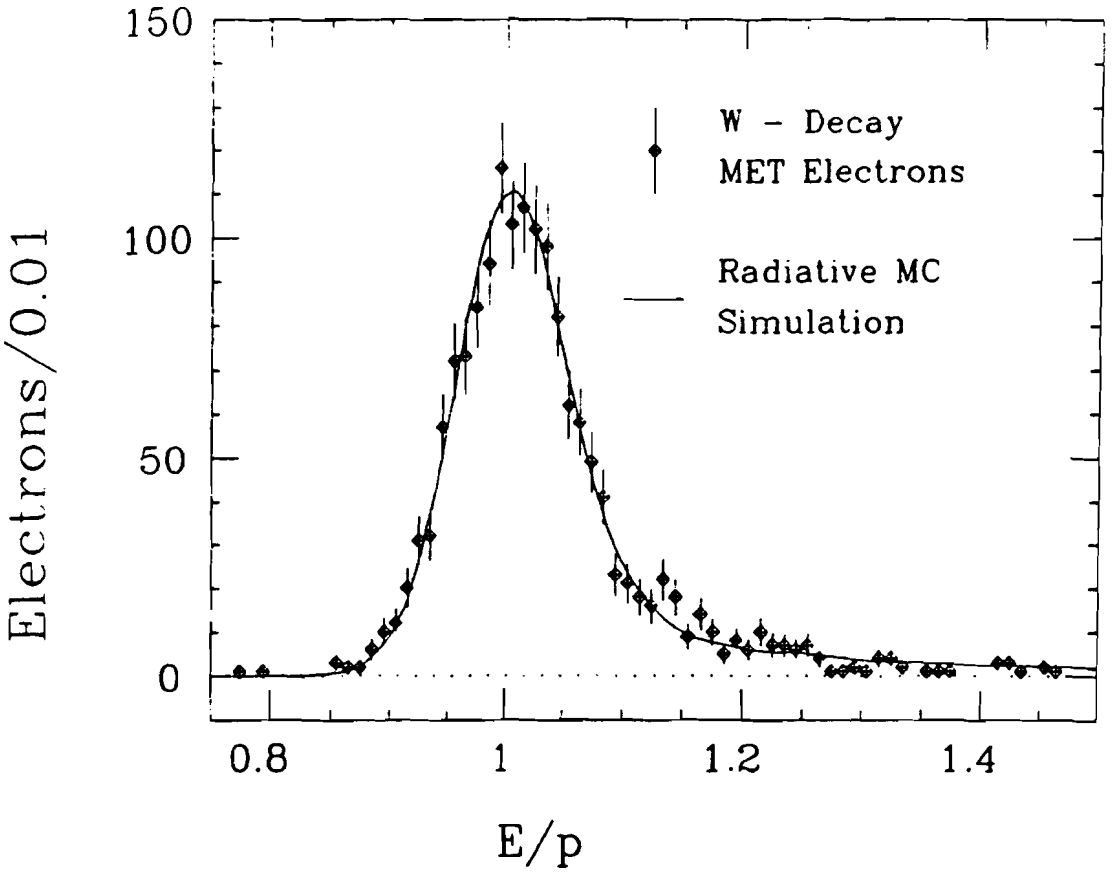

Figure 7. E/p distributions from data and a radiative Monte Carlo. The overall response scale is comparison of these two distributions. The distributions are normalized to equal area.

4.3.2 Strip Chamber Variables

As described in section 2.1, there is a gas proportional chamber (strip/wire chamber) located in the central EM calorimeter at shower maximum. This detector is used to define several variables for central electron selection. We use a chi–squared test (χ^2_{Strip}) to compare the shower shape in this detector in the Z view with the expected shower shape from electrons in testbeam data. The fit is to 11 points with 2 parameters and is rescaled by a factor which gave the χ^2 from testbeam data a mean of 1. This detector has a position resolution of 0.2 cm in both the Z view and azimuthal view. The strip cluster position is used in the definition of the good fiducial regions (see section 5.1). In addition, we define a strip – track match in both the Z view (ΔZ) and the azimuthal view ($\Delta R\phi$) between the strip cluster position and an associated track extrapolated to the strip chamber radius.

4.3.3 Lateral Shower Profile

A measurement of the lateral shower profile is also used to identify electrons. The variable *Lshr* is defined by

$$Lshr = 0.14 * \sum_i \frac{E_i^{Adj} - E_i^{Prob}}{\sqrt{0.14^2 * E + (\Delta E_i^{Prob})^2}} \tag{4.2}$$

where E_i^{Adj} is measured energy in the tower adjacent to the seed tower, E_i^{Prob} is the expected energy in that tower using the seed energy of the cluster, the impact point from the strip chamber, the event vertex, and a shower profile parametrization from testbeam data, E is the EM energy in the cluster, and ΔE_i^{Prob} is the error in E_i^{Prob} associated with a 1 cm error in the impact point measurement [44]. All energies are in GeV. The sum is over cluster towers adjacent to the seed tower in the same azimuthal wedge. *Lshr* gives a measurement of the lateral shower development and is different for electrons and jets.

4.4 Plug Electron Variables

4.4.1 Electron Response Corrections

Electron E_T in the plug calorimeter is defined using the energy measured in the calorimeter, corrected for several effects, and the angle from the position of the cluster in the detector, the location of the event vertex, and the beam direction. As described in section 2.1, the plug EM calorimeter is divided into quadrants. The global energy scale is set using one of these quadrants in an electron testbeam. A response map for the quadrant (taking into account tower–to–tower variations) is also derived from this testbeam data. The relative energy scale (quadrant–to–quadrant) is taken from comparing the $Z^0 \rightarrow e^+e^-$ invariant mass distributions (where one electron is in the CEM and the second in the PEM) and $W \rightarrow e\nu$ transverse mass distributions for each quadrant to those from the quadrant calibrated in the testbeam.

4.4.2 Additional Plug Electron Variables

Had/Em and *Iso* are criteria applied to electrons in all region of the calorimeter. We also use a lateral shower distribution in the plug region. This variable, denoted 3x3 χ^2 since it uses a 3x3 array of calorimeter cells and mimics a chi–squared test, measures the deviation of the shower from the predicted shower shape as seen in an electron testbeam. Since the full CTC tracking volume does not cover the plug region of the calorimeter (see figure 1), we are unable to use a track requirement in the CTC in our plug electron identification. The VTPC does give tracking information, but does not give a momentum measurement. We therefore use it to determine the presence of a charged particle track. Given the cluster position and the event vertex, we define a road where we would expect the electron to go through the VTPC active

region and look for hits on the wires along this road. The fraction of actual hits to expected hits is used to distinguish electrons from photons.

4.5 Forward Electron Variables

Electron E_T in the forward calorimeter is defined using the energy measured in the calorimeter, corrected for several effects, and the angle from the position of the cluster in the detector, the location of the event vertex, and the beam direction. As described in section 2.1, the forward EM calorimeter is divided into quadrants. The global energy scale is set using one of these quadrants in an electron testbeam and a comparison of the invariant mass distribution of the forward $Z^0 \rightarrow e^+e^-$ (where one electron is in the CEM and the second in the FEM) candidates to that of the central $Z^0 \rightarrow e^+e^-$ (where both electrons are in the CEM) candidates. The relative energy scale is set by comparison of the forward $Z^0 \rightarrow e^+e^-$ invariant mass distributions in the different quadrants and by a study of neutron induced pulses in each quadrant. This study assumes the flux of neutrons is independent of azimuth, so that the differential rate of neutrons above a threshold will be dependent upon the energy scale. Quadrant–to–quadrant corrections are checked by looking at the normalization of these rates in each quadrant. These corrections vary from -4% to +4%. A non-linearity correction taken from a study of testbeam and Z^0 data is also applied [45]. Electron identification in the forward region does not use any additional requirements beyond the Had/Em ratio and the Iso requirements.

4.6 Common Central Electron Sample

We define a sample of inclusive, high E_T, isolated central electrons (the common central electron sample) from which we choose W and Z^0 events. This sample has common selection efficiencies and backgrounds. We require that the candidate

Table 3. Summary of common central electron selection requirements

E_T	>	20.0 GeV
Iso	<	0.1
Had/Em	<	0.055 + 0.045×E/100
χ^2_{Strip}	<	15.0
$Lshr$	<	0.2
E/p	<	1.5
ΔZ	<	3.0 cm
$\Delta R\phi$	<	1.5 cm
$\|Z_{vert}\|$	<	60.0 cm

cluster have E_T > 20.0 GeV, Iso < 0.1, Had/Em < 0.055 + 0.045×E/100 where E is the energy of the cluster in GeV, χ^2_{Strip} < 15.0, and $Lshr$ < 0.2. From this sample, we add tracking requirements. We require a 3 dimensional track with E/p < 1.5, ΔZ < 3.0 cm, $\Delta R\phi$ < 1.5 cm, and that the Z vertex position as measured by the VTPC be within 60 cm of the nominal position. The requirements are summarized in table 3. The distributions of these variables are shown in figure 8. There are 5012 events which pass these requirements.

We additionally require that the event pass the electron trigger (we also had triggers based on transverse momentum imbalance and jet clusters which these events could pass) and that the central electron candidate be in a good fiducial region of the central detector (see section 5.1). From this sample, we define W and Z^0 candidate events. The basis of the W and Z^0 selection is then to look for the characteristics of the other lepton from the boson decay. For W 's, this lepton is a neutrino, so we look for a transverse energy imbalance. For Z^0's, this lepton is an electron so we look for the presence of another electromagnetic cluster.

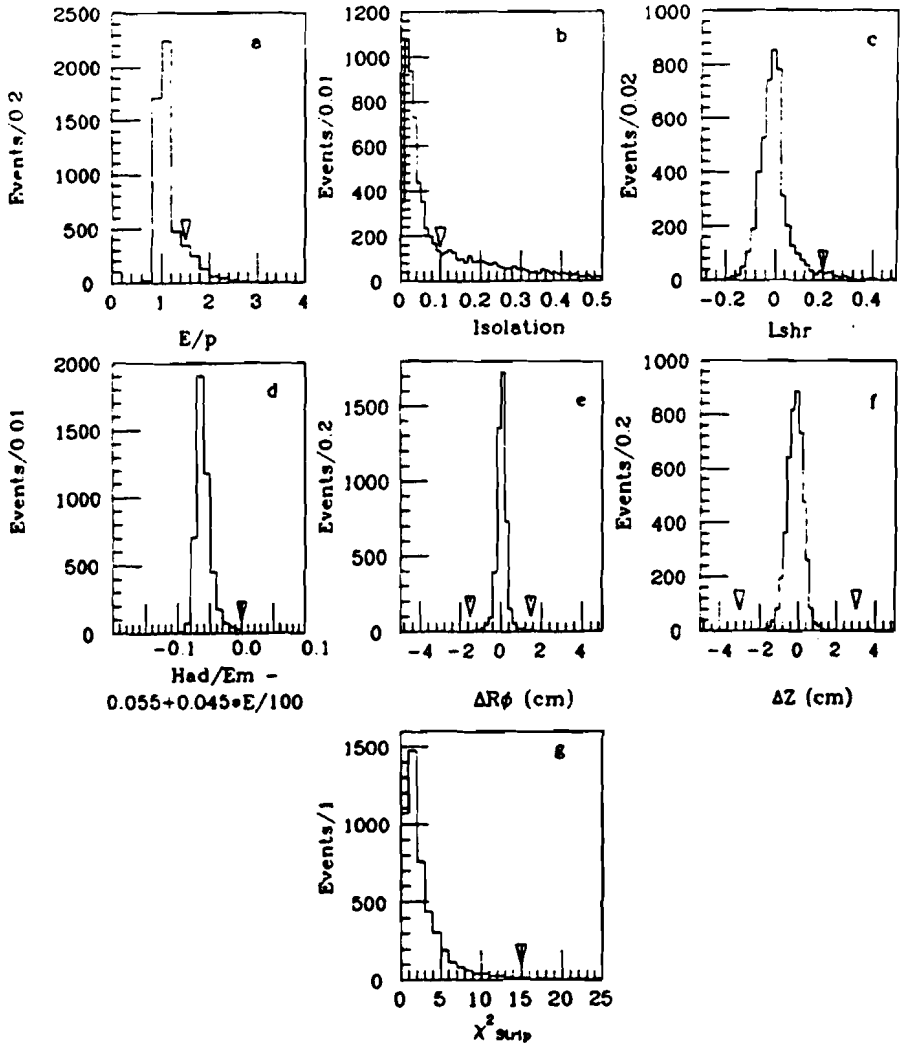

Figure 8. Distributions of the variables used in the central electron selection. These are the distributions after all cuts (see table 3) have been applied.

4.6.1 W *selection*

The missing E_T ($\not\!\!E_T$) is defined to be negative of the vector sum of transverse energy over the pseudorapidity range $|\eta| < 3.6$. The pseudorapidity range is restricted because the low beta quadrupoles of the Tevatron cover part of the azimuthal regions for $3.6 < |\eta| < 4.2$. To be included in the sum, the towers must pass an energy threshold requirement of 0.1 GeV in the CEM and CHA, 0.3 GeV in the PEM, 0.5 GeV in the PHA and FEM, and 0.8 GeV in the FHA [46]. The distribution of $\not\!\!E_T$ for electron events passing the trigger and fiducial requirements is shown in figure 9. The curve in the figure represents the expectation for the $\not\!\!E_T$ in W events. For W events, we require that $\not\!\!E_T > 20$ GeV. We also ask that the event not be consistent with being a Z^0 event (see below). There are 2664 events which pass these requirements.

4.6.2 Z^0 *selection*

We look for the presence of a second electromagnetic cluster in either the central, plug, or forward regions. The cluster must have $E_T > 10$ GeV, $Iso < 0.1$, $Had/Em < 0.1$, and be in a good fiducial region of the detector. There are additional selection requirements for the central and plug regions. For the central region, we require the presence of a good 3-d track and that $E/p < 2.0$. For the plug region, we ask that the $3x3$ $\chi^2 < 20.0$ and the VTPC hit fraction > 0.5. The distributions of these variables are shown in figure 10.

Once we have two selected clusters, we require that the invariant mass (see figure 11) of the clusters be between 70 and 110 GeV/c^2. There are 243 events which pass these requirements. The mass window introduces a bias, due to the presence of Drell-Yan events inside the window and Z^0 events outside the window. This bias will be discussed in further detail in section 8.

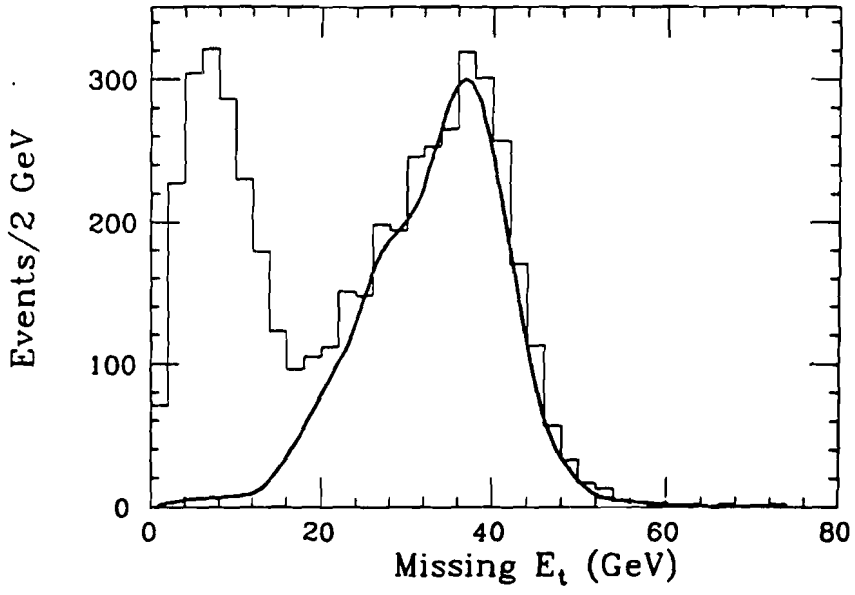

Figure 9. The $\not\!\!E_T$ distribution for events in the good central electron sample. The curve is a Monte Carlo expectation for W events.

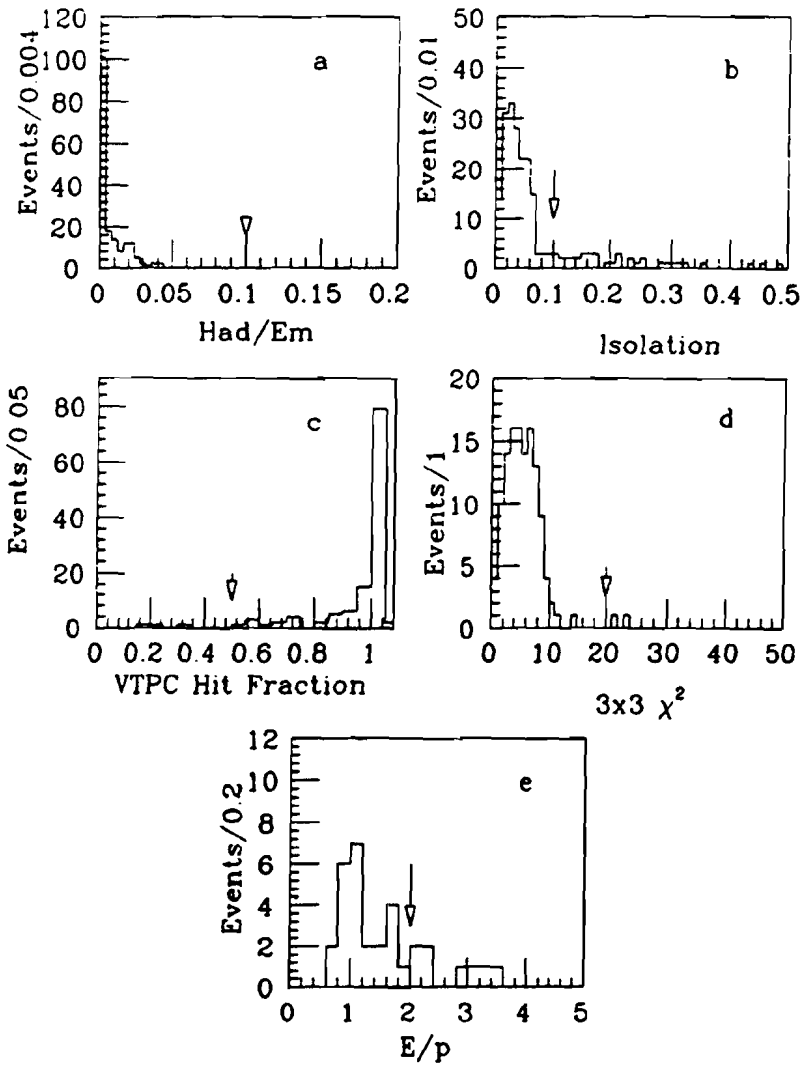

Figure 10. Distributions of the variables used in the second electron selection. These are the distributions after all cuts have been applied.

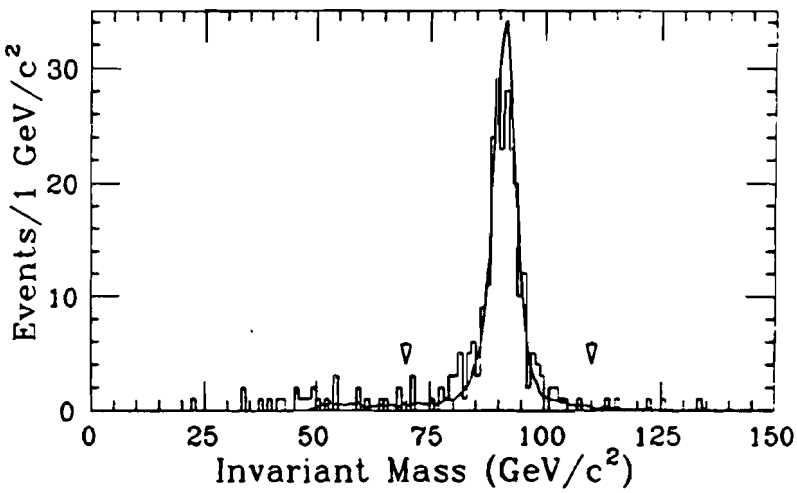

Figure 11. Invariant mass distribution for events with two electrons. In the Z^0 selection, we require the mass be in the window 70 - 110 GeV/c^2.

Chapter 5

Geometrical and Kinematical Acceptance

The boson selection efficiency can be factored into two terms, one for the geometrical acceptance and one for the efficiency of the electron and neutrino selection requirements. The geometrical acceptance accounts for the probability that the decay electrons will fall into the physical regions for which we will accept events, while the efficiency of the electron and neutrino selection requirements account for the probability that the electrons/neutrino will pass identification requirements. We include in the geometrical acceptance the probability that the electrons pass certain kinematical requirements. In this section, we discuss the geometrical and kinematical acceptance (hereafter referred to as acceptance). We begin with the definition of the good fiducial regions of our detector.

5.1 Fiducial Regions

The good fiducial regions are those parts of the detector where the calorimeter response to electrons is both well understood and relatively uniform. Although electrons are generally identifiable in other regions of the detector, the understanding

of the efficiency is not yet adequate for precision measurements. The good regions of the detector are away from detector boundaries.

As described in Section 2, CDF is constructed to be both azimuthally and forward-backward symmetric. A representation in η - ϕ space of one quadrant of the CDF detector is shown in figure 12, with the good fiducial regions for electrons marked. A detailed description of these regions follows.

In the eta coordinate, we require that the electron be in one of the following regions: $0.05 < |\eta| < 1.0$, $1.3 < |\eta| < 2.2$, or $2.4 < |\eta| < 3.7$. The region $|\eta| < 0.05$ corresponds to the $\theta = 90°$ crack, where the two halves of the central calorimeter come together. The region $1.0 < |\eta| < 1.3$ corresponds to the boundary of the central and plug calorimeters. Due to the different shaped calorimeter elements and the overlap between calorimeter elements at the boundaries giving rise to variations in response, this region is not included. The region $2.2 < |\eta| < 2.4$ corresponds to where the plug and forward calorimeter coverage overlaps. Again the changing response at the boundary excludes this region.

For electrons within the central region, the selection is based on the strip cluster Z position (i.e., along the beam direction). We require that the strip cluster position be more than 9 cm and less than 217 cm from the $\eta = 0$ plane. The strip chambers cover the region 6 cm $< Z <$ 239.4 cm and the active region of the calorimeter covers 4.2 cm $< Z <$ 246.0 cm [41].

For electrons in the plug and forward calorimeters, the selection is based on the location of the seed tower in the cluster. Towers in these calorimeters are segmented into roughly 0.1 units of η. In the plug region, we require that the seed tower be more than two towers away from the calorimeter η boundaries. In the forward region we require that the seed tower be more than 5 towers away from the large η boundary (closer to the beamline) but make no requirement near the small η boundary.

In the ϕ coordinate, the selection differs depending upon the detector region. At the depth of the strip/wire chamber in the central region, the wedge has a width

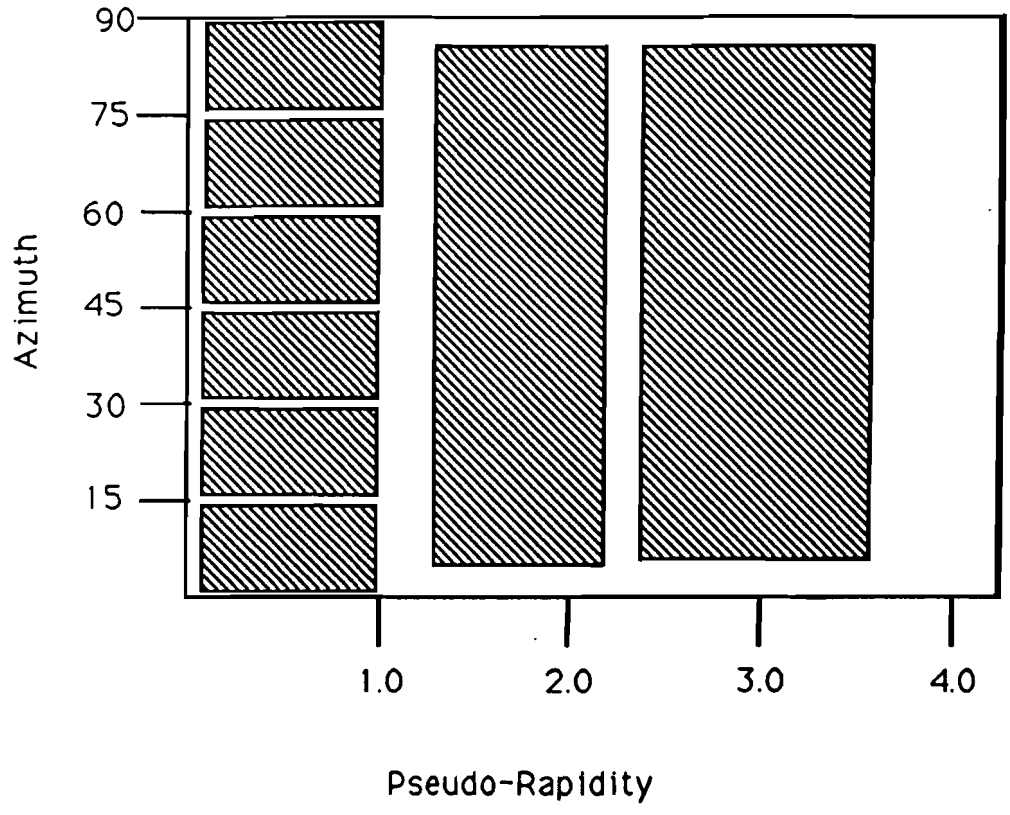

Figure 12. One quadrant of the CDF detector in η - ϕ space. The good fiducial regions for electrons are shaded.

of 48.4 cm, the strip chambers extend to within 1.7 cm of the wedge boundary and the active region of the calorimeter extends to within 1.1 cm [41]. In this region, we require that the strip cluster position be more than 3.2 cm from the wedge boundary.

For the plug and forward regions, we require that the seed tower of the cluster not be within 5° of the quadrant boundaries. These calorimeters are segmented into towers of 5° in ϕ, so that this requirement excludes the towers adjacent to the boundary.

In addition to these symmetric boundary regions, we have several small irregular regions which are excluded. The region $0.77 < \eta < 1.0$, $75° < \phi < 90°$ is not instrumented — it is the penetration for the cryogenic connections to the superconducting solenoid. In the plug calorimeter, there were a small number of known regions with dead channels ($\sim$ 2%) and we require that the seed tower not be in one of these regions.

5.2 Detector Model

A simple detector model is used for the study of acceptances. It is not a complete simulation, using only the lepton 4–vectors, since the acceptance is defined by requiring the electrons from the boson decays pass only certain geometrical and kinematical requirements. Electron selection efficiencies are studied from the data and are discussed in section 6.

In the model, an event vertex is chosen from a Gaussian distribution with $\sigma = 30$ cm, truncated at 2σ. The decay electrons are propagated from the vertex to the calorimeters including the effects of the magnetic field, and fiducial cuts are applied to the position of the electrons as in the data. Electron energies are smeared using Gaussians of the nominal calorimeter resolutions (see section 2.1). We require that there be one central electron with $E_T > 20$ GeV in a good fiducial region for both W and Z^0 events. For Z^0 events, we additionally require that there

be a second electron with $E_T > 10$ GeV in a good fiducial region in any of the calorimeters.

5.3 Monte Carlo Generators

We use a zeroth order Monte Carlo which includes only the Drell–Yan diagram $q + \bar{q} \rightarrow W(Z^0)$ (figure 13) to generate 4–vectors for the leptons in the boson decays. It includes polarization effects and the correct matrix element for the decays $W \rightarrow e\nu$ and $Z^0 \rightarrow e^+e^-$. The bosons are generated from a relativistic Breit-Wigner line shape truncated at $\pm$ 2 widths (the results are found to be independent of this cut). We do not include the photon diagrams in the Z^0 Monte Carlo, but correct for the effects later.

We take as input structure function parametrizations by Martin et al. (MRSB) [47], Duke and Owens with $\Lambda_{QCD} = 0.2$ GeV (DO1) [48], and Eichten et al. with $\Lambda_{QCD} = 0.2$ GeV (EHLQ1) [49]. Since the bosons from this Monte Carlo are generated with zero transverse momentum, the transverse momentum spectrum measured from Z^0 candidate events (where the boson 4–vector is reconstructed) is used as an input distribution (figure 14). Systematic uncertainties due to including only first order diagrams are discussed in the following section.

We also use the ISAJET [50] and PAPAGENO [51] Monte Carlos as event generators. These Monte Carlos allow for the inclusion of higher order diagrams such as $q+g \rightarrow W(Z^0)+q$ and $q+\bar{q} \rightarrow W(Z^0)+g$ (figure 15) in the generation. Although these generators are slower than the Monte Carlo described above, they provide a valuable check on the results. These checks are documented in the following section.

5.4 Acceptance Results and Systematics

We define the acceptances for W and Z^0 events as follows:

$$A_W = \frac{\#\text{ events with electron in good central fiducial region, } E_T > 20}{\#\text{generated events}}$$

$$A_Z = \frac{\#\text{ events with 1 electron in good central fiducial region, } E_T > 20 \text{ and a second electron in any good fiducial region, } E_T > 10}{\#\text{generated events}}$$

In addition, for Z^0 events we define the following variables:

$$F_{cc} = \frac{\#\text{ events with second electron in central fiducial region}}{\#\text{ accepted events}}$$

$$F_{cp} = \frac{\#\text{ events with second electron in plug fiducial region}}{\#\text{ accepted events}}$$

$$F_{cf} = \frac{\#\text{ events with second electron in forward fiducial region}}{\#\text{ accepted events}}$$

These variables represent the fraction of accepted events which have both electrons in the central region (F_{cc} central- central events), one electron in the central region and the second in the plug region (F_{cp} central-plug events), or one electron in the central region and the second in the forward region (F_{cf} central- forward events). They are used in the calculation of the overall selection efficiency for Z^0 events.

In Table 4 we show the values for A_W and A_Z, where we have used our zeroth-order Monte Carlo with p_T taken from the (smoothed) p_T distribution of the Z^0 candidates (see figure 14). The quoted errors in the table are statistical only. One can see that A_W varies at the 3% level when changing structure functions, whereas A_Z is more stable. We take the uncertainties on A_W and A_Z due to the choice of structure functions to be $\pm$ 3% and $\pm$ 0.8% respectively.

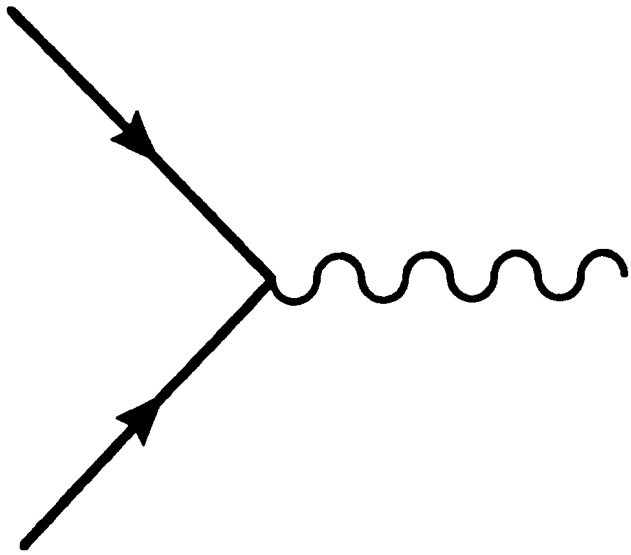

Figure 13. Feynman diagrams used in zeroth order Monte Carlo.

Table 4. Acceptances and detector fractions for W and Z^0 for various sets of parton structure functions (P.S.F.)

P.S.F	$A_W(\%)$	$A_Z(\%)$	F_{cc}	F_{cp}	F_{cf}
MRSB	35.2 ± 0.1	37.1 ± 0.1	0.40	0.47	0.13
DO1	34.0 ± 0.1	37.0 ± 0.1	0.40	0.46	0.14
EHLQ1	35.9 ± 0.1	37.2 ± 0.1	0.39	0.47	0.14

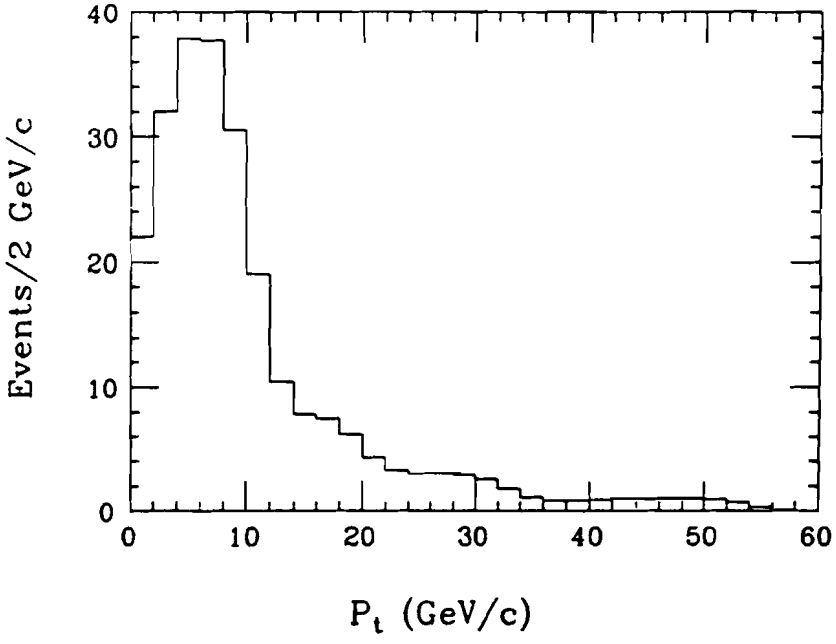

Figure 14. p_T distribution input to zeroth order Monte Carlo.

The W acceptance is also a function of M_W, changing by approximately 2.3% (of itself) for a 1 GeV/c^2 change in M_W. The assumed masses were M_W = 80.0 GeV/c^2 and M_Z = 91.1 GeV/c^2. We have used $\sin^2\theta_W = 0.229 \pm 0.007$ [52] which implies a 360 MeV/c^2 uncertainty in M_W (given the fixed M_Z). We therefore assign an additional $\pm$ 0.8% uncertainty to A_W.

The assumed p_T distribution has little effect on the acceptances. Figure 16 shows A_W and A_Z as a function of p_T. Scaling the p_T distribution of figure 14 by $\pm$ 20% (which we feel more than covers the possible uncertainty in the overall momentum distribution) changes the acceptances by less than 1%. We take $\pm$ 1% as the uncertainty due to the choice of p_T.

Finally, higher order QCD corrections are expected to alter the rapidity distributions (see, for example [22]) and therefore the acceptances. ISAJET with only the lowest order Drell–Yan diagram (figure 13), where events from this process pick up transverse momentum from initial state radiation, gives the same answer for the acceptances as our Monte Carlo. Running ISAJET with only the higher order diagrams (figure 15) changes A_W and A_Z by approximately +8.4% and +3.8%, respectively.

We also have studied the effect of higher order corrections by running PAPAGENO with zeroth and first order diagrams. PAPAGENO with only the lowest order Drell–Yan diagram does not give transverse momentum to the bosons. If we again use the p_T distribution from our candidate Z^0 events, we find that the acceptance is the same as from our Monte Carlo. Running PAPAGENO with the next order diagrams only and a lower cutoff on the parton p_T of 8 GeV/c, we find that A_W increases by 3.6% and A_Z by 2.1%.

Our Monte Carlo reproduces the leading order calculations from ISAJET and PAPAGENO, but QCD corrections seem to alter the leading order rapidity distributions. Figure 17 shows the rapidity distributions for the W boson from zeroth order and first order calculations. Since the order α_s and higher diagrams contribute of

Table 5. Contributions to systematic uncertainties in the calculation of acceptances

Source of Systematic Error	Uncertainty in A_W	Uncertainty in A_Z
Structure Functions	±3.0%	±0.8%
Mass	±0.8%	
p_T	±1.0%	±1.0%
Higher Order Terms	±2.5%	±1.1%
Total	±4.1%	±1.7%

order 30% to the total cross sections, we choose to assign a systematic error to A_W and A_Z equal to 30% of the predicted ISAJET increase in acceptance (i.e., we take ± 2.5% for A_W and ± 1.1% for A_Z). The systematic uncertainties in the W and Z^0 acceptances are summarized in Table 5.

5.5 Final Values for the W and Z^0 Geometrical Acceptances

We choose to use MRSB structure functions and the results from our zeroth-order Monte Carlo for the values of A_W and A_{Z^0}. For the W acceptance, the prediction of this set of structure functions falls in between the values of DO1 and EHLQ1. In the Z^0 case, the acceptances are almost identical (see Table 4). The values are then:

$$A_W = 35.2 \pm 1.5\ \%$$
$$A_{Z^0} = 37.1 \pm 0.7\ \%$$

The acceptance is a combination of kinematical and geometrical requirements. In the case of the W 's, the requirement that the electron pass the kinematical

requirement is $\sim$ 81% efficient. Of the electrons that satisfy this criterion, $\sim$ 57% of them are in the central region and, of these, $\sim$ 76% are in a good fiducial region. In the case of the Z^0's, the kinematical requirements for the electrons are $\sim$ 88% efficient. Of events satisfying these criteria, $\sim$ 80% have electrons in the central region. Of these central electrons, $\sim$ 83% are in a good fiducial region. Requiring that the second electron be in a good fiducial region anywhere in the detector is then $\sim$ 64% efficient.

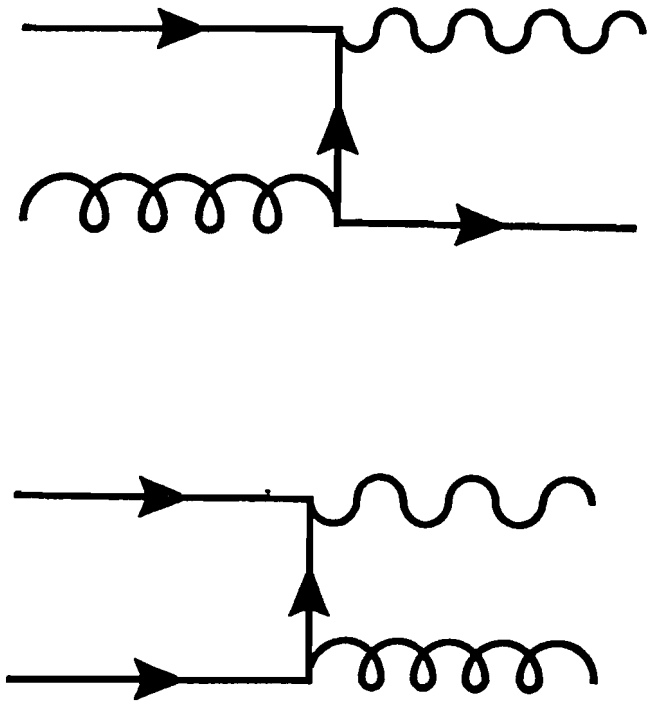

Figure 15. Feynman diagrams used in higher order Monte Carlo.

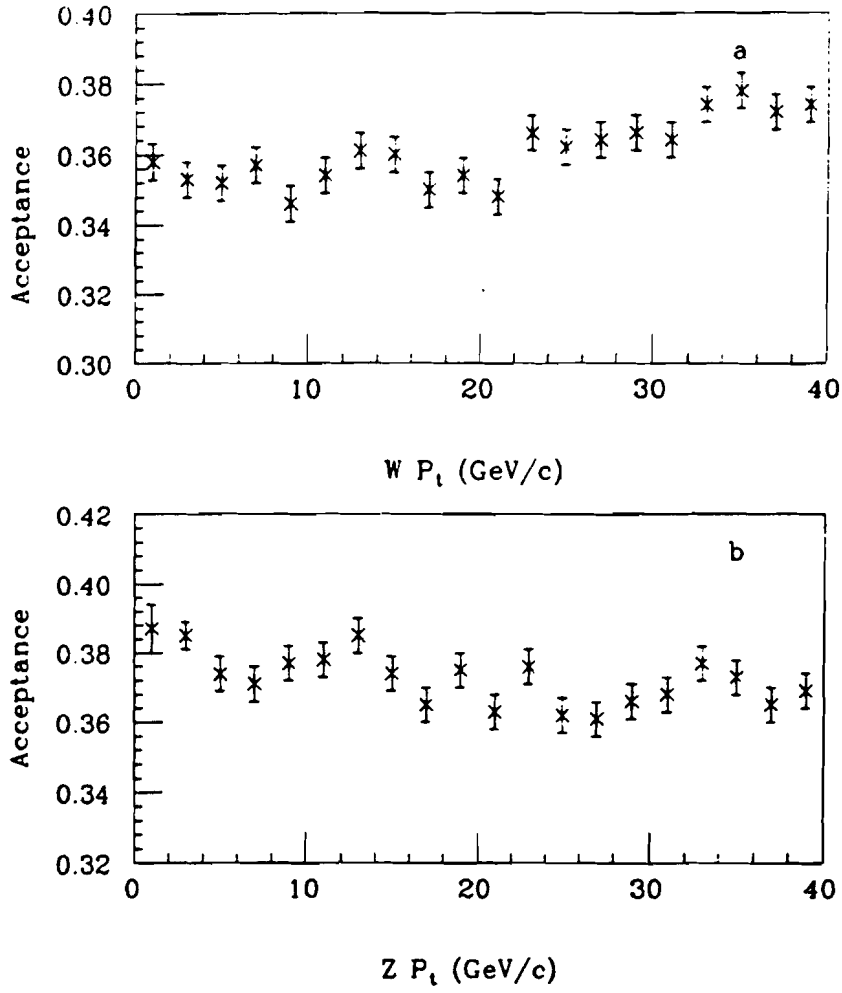

Figure 16. The acceptance for (a) W and (b) Z^0 events as a function of the boson p_T. The majority of the data has $p_T < 20.0$ GeV/c.

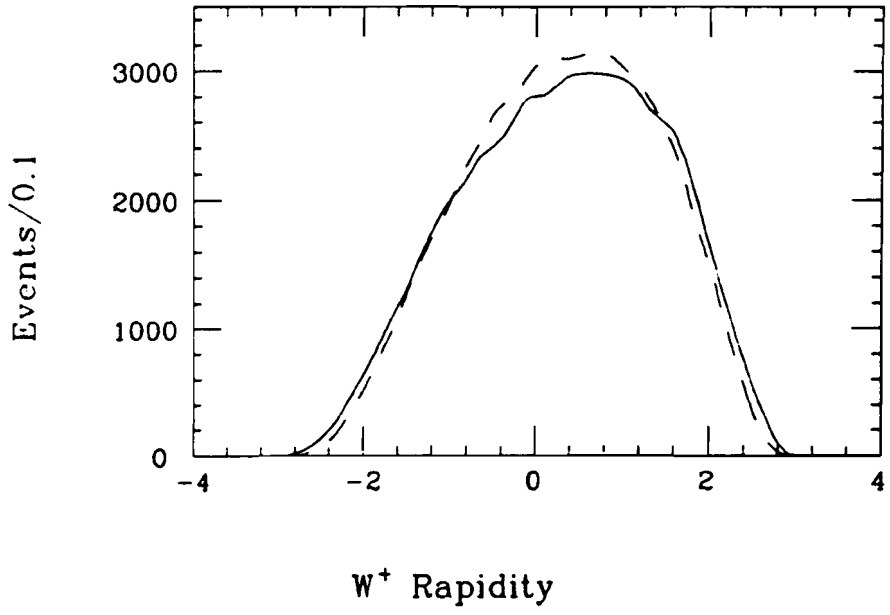

Figure 17. Rapidity distributions for W bosons from zeroth and first order calculations. We have used our own Monte Carlo for the zeroth order and ISAJET for the first order calculation.

Chapter 6

Selection Efficiencies

The efficiency studies can be broken down into two pieces, one representing the electron selection efficiencies and the other representing the $\not\!\!E_T$ selection efficiency. The electron selection efficiencies are common to both the W and Z^0 cross section measurements and will be discussed first.

6.1 Electron Identification Efficiency

The efficiencies for the electron selection requirements are studied directly from data. To measure the efficiencies properly one would like an unbiased, background free sample of W's and Z^0's decaying to electrons. Unfortunately, cuts which are necessary to lower the background may also bias the distributions. We attempt to measure the efficiencies in a number of ways to cross check the results.

The first way is by selecting an independent sample of W events using global event topologies rather than electron selection, tagging the decay through the presence of the ν (the $\not\!\!E_T$ selected electron sample). We ask that there be a large transverse momentum imbalance and that this imbalance be significant in comparison to the total energy flow in the event. In addition, we ask that there be one and

only one cluster of energy in the event and that this cluster be predominantly in the electromagnetic portions of the calorimeter. The process $W \rightarrow e\ \nu$ has all of these characteristics. This gives us a sample of high p_T electrons without the electron cuts applied.

As a second method, we use a sample of $Z^0 \rightarrow e^+e^-$ events (the Z^0 selected electron sample), selected on the basis of one good electron candidate and an invariant mass constrained to the Z^0 mass. By looking at the characteristics of the second electron in the event, we are able to measure the electron identification efficiencies in a second unbiased fashion.

We require for the $\not\!\!E_T$ selected sample that $\not\!\!E_T > 20$ GeV, $|Z_{vert}| < 60$ cm, and $\delta\ \not\!\!E_T \equiv \frac{\not\!\!E_T}{\sqrt{\sum E_T}} > 2.7$, which is a cut of more than 4.5σ in azimuthally symmetric events where the $\not\!\!E_T$ comes from measurement resolution. The $\sum E_T$ is the scalar sum of all transverse energy over the same η range as the $\not\!\!E_T$ sum. We require that there be one cluster in the event with $E_T > 5$ GeV, that Had/Em is < 0.125 for this cluster, and that the cluster be in a good fiducial region. If the cluster is in the plug or forward regions, we also require that the transverse mass [53] be > 50 GeV/c^2.

For the Z^0 selected sample we require the presence of one good central electron, as defined in section 4.6, a second cluster with $E_T > 10$ GeV, with the invariant mass of the two clusters in the window 81 - 101 GeV/c^2. Figure 18 shows the invariant mass distribution for these events. The second cluster is required to be in a good fiducial region.

From these samples, we measure the electron identification efficiencies. Tables 6, 7, 8, and 9 show the individual efficiencies for each of the cuts in the event selection and the combined efficiency for the entire set of cuts from both the $\not\!\!E_T$ selected and Z^0 selected samples. We use the efficiency of the combined set of cuts (which is not equal to the multiplication of the individual cuts) to account for correlations which might exist. The efficiencies for both samples are in reasonable agreement. The combined efficiency from the $\not\!\!E_T$ (Z^0) selected sample for the com-

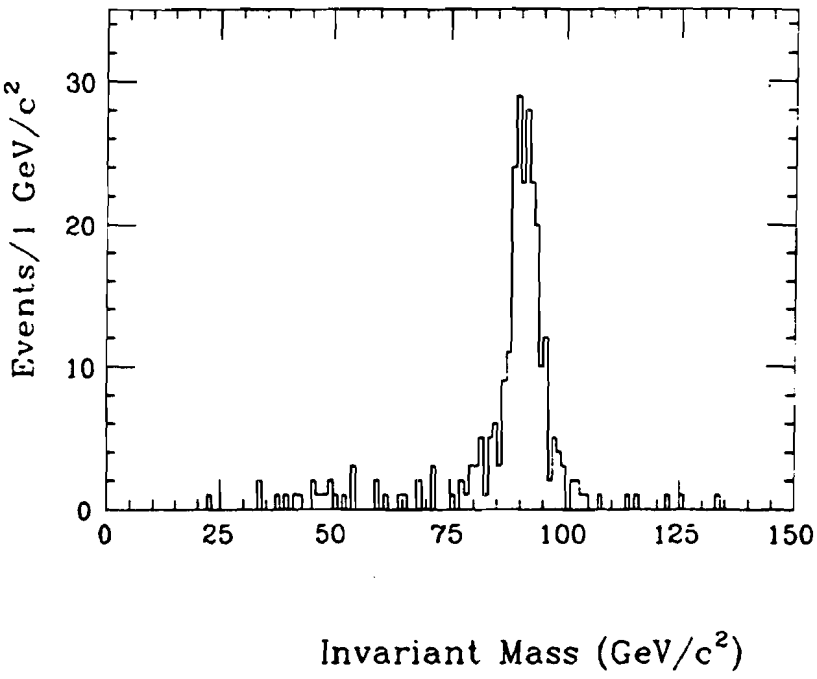

Figure 18. Invariant mass distribution for events with one well identified central electron and a second cluster. The window 81 — 101 GeV/c^2 is used in the selection of events for the efficiency measurement.

Table 6. The individual and combined electron selection efficiencies for the $\not\!\!E_T$ selected sample and the Z^0 samples for the common central electron selection, c_1

Quantity	$\not\!\!E_T$ sample (1187 events)	Z^0 sample (87 events)
Iso	0.96 ± 0.01	0.97 ± 0.01
Had/Em	0.99 ± 0.01	0.99 ± 0.01
χ^2_{Strip}	0.97 ± 0.01	0.97 ± 0.01
Lshr	0.97 ± 0.01	0.99 ± 0.01
E/p	0.93 ± 0.01	0.93 ± 0.02
ΔZ	0.98 ± 0.01	0.99 ± 0.01
$\Delta R\phi$	0.97 ± 0.01	0.97 ± 0.01
Trigger	0.973 ± 0.005	0.973 ± 0.005
All	0.84 ± 0.03	0.85 ± 0.03

Table 7. The individual and combined electron selection efficiencies for the $\not\!\!E_T$ selected sample and the Z^0 samples for the loose central electron selection, c_2

Quantity	$\not\!\!E_T$ sample (1187 events)	Z^0 sample (87 events)
Iso	0.96 ± 0.01	0.97 ± 0.01
Had/Em	0.99 ± 0.01	0.99 ± 0.01
E/p	0.97 ± 0.01	0.96 ± 0.02
All	0.93 ± 0.03	0.93 ± 0.03

Table 8. The individual and combined electron selection efficiencies for the $\not\!\!E_T$ selected sample and the Z^0 samples for the plug electron selection, p

Quantity	$\not\!\!E_T$ sample (500 events)	Z^0 sample (76 events)
Iso	0.96 ± 0.01	0.93 ± 0.03
Had/Em	0.99 ± 0.01	0.99 ± 0.01
$3x3\ \chi^2$	0.94 ± 0.01	0.99 ± 0.01
VTPC Hit Fraction	0.93 ± 0.02	0.96 ± 0.02
All	0.90 ± 0.03	0.92 ± 0.03

Table 9. The individual and combined electron selection efficiencies for the $\not\!\!E_T$ selected sample and the Z^0 samples for the forward electron selection, f

Quantity	$\not\!\!E_T$ sample (135 events)	Z^0 sample (19 events)
Iso	0.91 ± 0.02	0.90 ± 0.07
Had/Em	1.00 ± 0.01	0.95 ± 0.05
All	0.91 ± 0.03	0.89 ± 0.07

mon central electron selection (c_1) is 0.84 ± 0.03 (0.85 ± 0.03), for the loose central electron selection (c_2) is 0.93 ± 0.03 (0.93 ± 0.03), for the plug electron selection (p) is 0.90 ± 0.03 (0.92 ± 0.03), and for the forward electron selection (f) is 0.91 ± 0.03 (0.89 ± 0.07). We take as final values for these efficiencies:

$$\begin{aligned} c_1 &= 0.84 \pm 0.03 \\ c_2 &= 0.93 \pm 0.03 \\ p &= 0.91 \pm 0.03 \\ f &= 0.91 \pm 0.04 \end{aligned}$$

We have increased the uncertainty in the forward electron selection efficiency from the statistical level of 0.03 to 0.04 because of worries about background in the $\not\!\!E_T$ sample used to measure the efficiency. Background in the sample would cause an underestimation of the selection efficiency.

We also use the $\not\!\!E_T$ selected sample to measure our trigger efficiency. In addition to the electron trigger discussed in section 3, we had a trigger which looked for an E_T imbalance in the calorimeter. This trigger is independent of the electron trigger and we expect some fraction of W events also to pass this trigger. After identifying an electron in the $\not\!\!E_T$ sample, we then use the sample to measure the efficiency of the electron trigger. The electron trigger efficiency is measured to be 0.973 ± 0.005.

6.2 $\not\!\!E_T$ Selection Efficiency

To measure the efficiency of the $\not\!\!E_T$ requirement, we use the PAPAGENO event generator and a full detector simulation. In other studies, the predictions of this Monte Carlo for kinematical properties of W + jet events agree well with the distributions seen in data [54].

The $\not\!\!E_T$ selection efficiency (ϵ_ν) is defined to be the probability that $\not\!\!E_T > 20$ GeV

Table 10. The $\not\!\!E_T$ efficiency as a function of the number of jets with $E_T > 10$ GeV in the event and the fraction of events with 0, 1, or ≥ 2 jets

	0 Jets	1 Jet	≥ 2 Jets
ϵ_ν	0.98 ± 0.01	0.90 ± 0.02	0.88 ± 0.02
Fraction (data)	72%	20%	8%
Fraction (Monte Carlo)	74%	21%	5%

given that the electron has $E_T > 20$ GeV. We study this probability as a function of the number of energetic jets with detected $E_T > 10$ GeV (see reference [55] for the definition of a jet) besides the electron candidate in these events. We find that ϵ_ν decreases with the presence of additional energetic jets in the event. This correlation comes from the broadening of the $\not\!\!E_T$ resolution as a function of the total energy in the event.

We use the event fractions as seen in the data for this weighting. We find that ϵ_ν is correlated with the number of jets and that the Monte Carlo reproduces the cluster fractions within reasonable agreement. Table 10 summarizes the information on ϵ_ν. The final value for the $\not\!\!E_T$ efficiency is $\epsilon_\nu = 0.96 \pm 0.02$.

6.3 Final Selection Efficiencies

The total efficiency term for the W selection is given by $\epsilon_W = \epsilon_\nu \cdot c_1$, accounting for both the $\not\!\!E_T$ and electron selection efficiencies. For this analysis, $\epsilon_W = 0.81 \pm 0.04$.

The efficiency term for the Z^0 selection is a combination of the electron selection efficiencies and the detector fractions (as defined in section 5). It is defined as:

Table 11. The selection efficiencies for the W and Z^0 samples

	Efficiency
c_1	0.84 ± 0.03
c_2	0.93 ± 0.03
p	0.91 ± 0.03
f	0.91 ± 0.04
ϵ_ν	0.96 ± 0.02
ϵ_W	0.81 ± 0.04
ϵ_Z	0.80 ± 0.03

$$\epsilon_Z = F_{cc} \cdot c_1 \cdot (2c_2 - c_1) + F_{cp} \cdot c_1 \cdot p + F_{cf} \cdot c_1 \cdot f, \tag{6.1}$$

where F_{cc}, F_{cp}, and F_{cf} are the expected fractions of events with the second electron in the central, plug, and forward regions from the acceptance studies. In Eq (6.1), we have neglected the contribution to ϵ_Z from events where the second central electron has 10 GeV $<$ E_T $<$ 20 GeV because the acceptance for this class of events is negligible. The term $2c_2 - c_1$ arises because Z^0 events with both electrons in the central region can have either electron satisfy the common central electron requirement. The final value for ϵ_Z is 0.80 ± 0.03 [56]. The complete efficiencies are summarized in table 11.

Chapter 7

Backgrounds

High p_T, isolated electrons come predominantly from the decay of W and Z^0 bosons, but there are other processes which have such a signal. It is necessary to understand the contributions from other processes in the selection of W and Z^0 events.

7.1 W Backgrounds

Though the selection of W events is relatively straightforward, there are several processes which can mimic the signal of a high p_T, isolated electron and the presence of missing transverse energy. There are contributions to these processes from both physics processes and from detector effects.

We consider backgrounds from QCD processes such as quark-quark or gluon-gluon scattering (multijet events) and heavy quark production. Given the prevalence of these processes in comparison to W production at the Q^2 scale of interest, even topologies with small probabilities can contribute to the W sample. The background from QCD processes enters when one parton looks to be an isolated electron while the other parton, through fluctuations in fragmentation and the detector response, mimics the neutrino. The isolated electron can come from either a fluctuation in the parton fragmentation or, in the case of a heavy quark decay, can be a real electron.

We study this background using the isolation distributions of the W sample and a separate sample of electron events. For this second sample of electron events, we do not use an isolation requirement as one of the selection criteria. Otherwise, we use the same event selection as outlined in section 4.6. Since we want the background sample to contain no W event contamination, we require that the $\not\!\!E_T$ for this sample be less than 10 GeV. If the $\not\!\!E_T$ and isolation are correlated, this requirement could bias the background sample. To first order we expect no correlation between these variables to exist because the regions of the events which determine the isolation and $\not\!\!E_T$ characteristics are physically separated from each other. In dijet events, one jet fluctuates to fake an electron while fluctuations in the opposite jet dominate the $\not\!\!E_T$. In $\bar{b}b$ events, the c quark jet associated with the electron can contribute to both the $\not\!\!E_T$ and the isolation; however, since the the electron is required to have a high transverse momentum, the c quark jet is expected to be much softer than the opposite jet and not contribute much to the $\not\!\!E_T$.

To test this hypothesis, we selected events with a good electron (passing all the central electron cuts except the isolation requirement), and plot the event $\not\!\!E_T$ versus the isolation of the electron (see figure 19). The region with $\not\!\!E_T > 20$ GeV and $Iso < 0.1$ shows a clustering which is the W signal. In events with $\not\!\!E_T > 20$ GeV, we see a tail in the isolation distribution stretching out to high values of Iso, but there is no visible correlation between the two variables.

To estimate the background contribution we define 3 samples from the non-isolated electron sample:

- Events with $\not\!\!E_T > 20$ GeV (the $\not\!\!E_T > 20$ sample).
- Events with $\not\!\!E_T < 10$ GeV and a jet with $E_T > 10$ GeV (control sample 1)
- Events with $\not\!\!E_T < 10$ GeV and a jet with $E_T > 20$ GeV, which is a subset of control sample 1 (control sample 2).

In all of these samples, we reject events which pass the Z^0 selection. Figure 20 shows

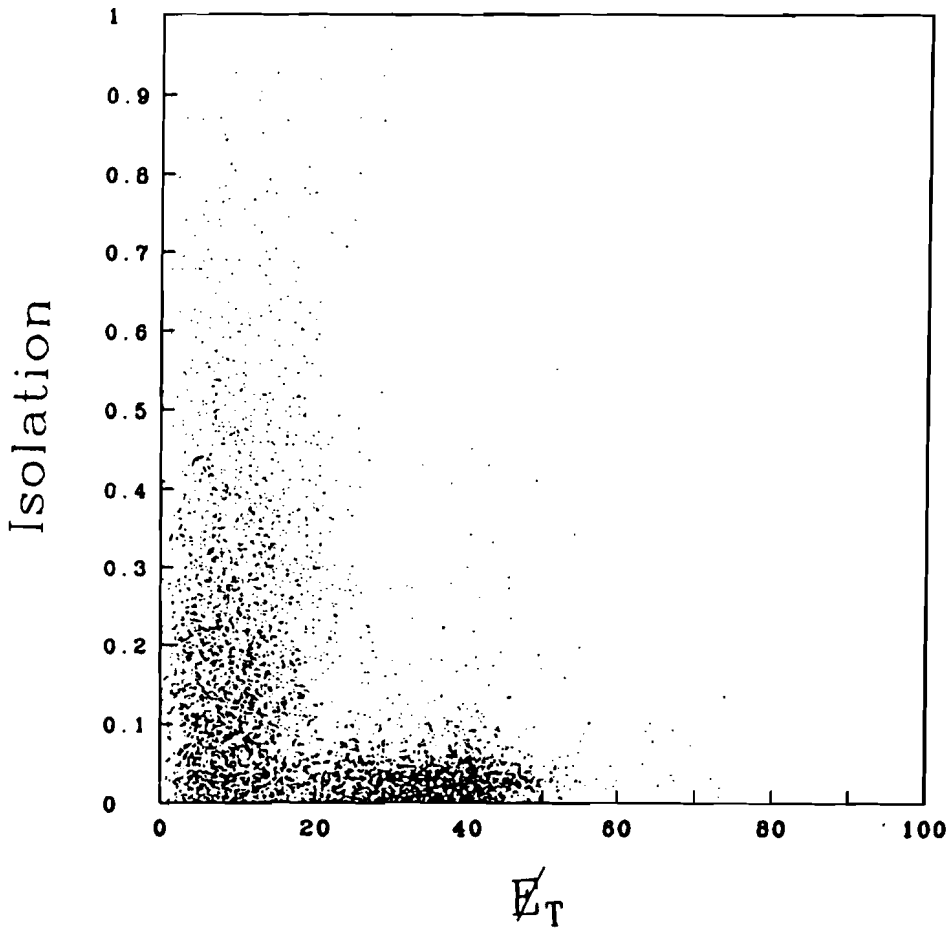

Figure 19. $\not\!\!E_T$ vs. *Iso* for the common central electron sample, where we have not used an *Iso* requirement. The clustering with $\not\!\!E_T > 20$ GeV and $Iso < 0.1$ is the W sample.

the isolation distributions for the three samples. We then estimate the background using the equation:

$$\frac{W \text{ background}}{\#\, Iso > 0.3 \text{ in the } \not\!\!E_T > 20 \text{ sample}} = \frac{\#\, Iso < 0.1 \text{ in control sample 1 or 2}}{\#\, Iso > 0.3 \text{ in control sample 1 or 2}} \tag{7.1}$$

taking the average of the answers using the two control samples. We find this background to be 100 ± 50 events.

We next consider the process $Z^0 \rightarrow e^+e^-$ with one electron detected and the other not identified as an electron in the calorimeter (due to detector effects such as cracks or poor EM response). We would then see an electron in conjunction with $\not\!\!E_T$. In the region $|\eta| < 1.1$ where we have good tracking we can use the presence of a track to reject such events, but if the second electron from the Z^0 decay is outside this region we are unable to reject the event. We have used ISAJET and a full detector simulation to estimate this background, where we have normalized to the number of Z^0 events in our sample. From this study, we estimate a background of 40 ± 15 events from this process.

We also consider the process $Z^0 \rightarrow \tau^+\tau^-$, where one τ decays into an electron and there is a large amount of $\not\!\!E_T$ in the detector. We have again used ISAJET and a full detector simulation to estimate this background. Taking into account the branching fraction of $\tau \rightarrow e\, \nu\, \nu$ and normalizing to the number of events in our $Z^0 \rightarrow e^+e^-$ sample, we estimate this background to be 8 ± 4 events.

We consider the decay of heavy top into real W's as a background process. Since we see no evidence for any such decay with the top mass less then 89 GeV/c^2 [57], we take the background contribution to be 0, but with an error equal to the number of events in the W sample for a 90 GeV/c^2 top mass, assuming a 150 pb cross section [58]. Using the ISAJET program and a full detector simulation, we estimate a background of 30 events from the decay

$$t \rightarrow Wb \qquad W \rightarrow e\, \nu$$
$$\bar{t} \rightarrow W\bar{b} \qquad W \rightarrow \text{anything.}$$

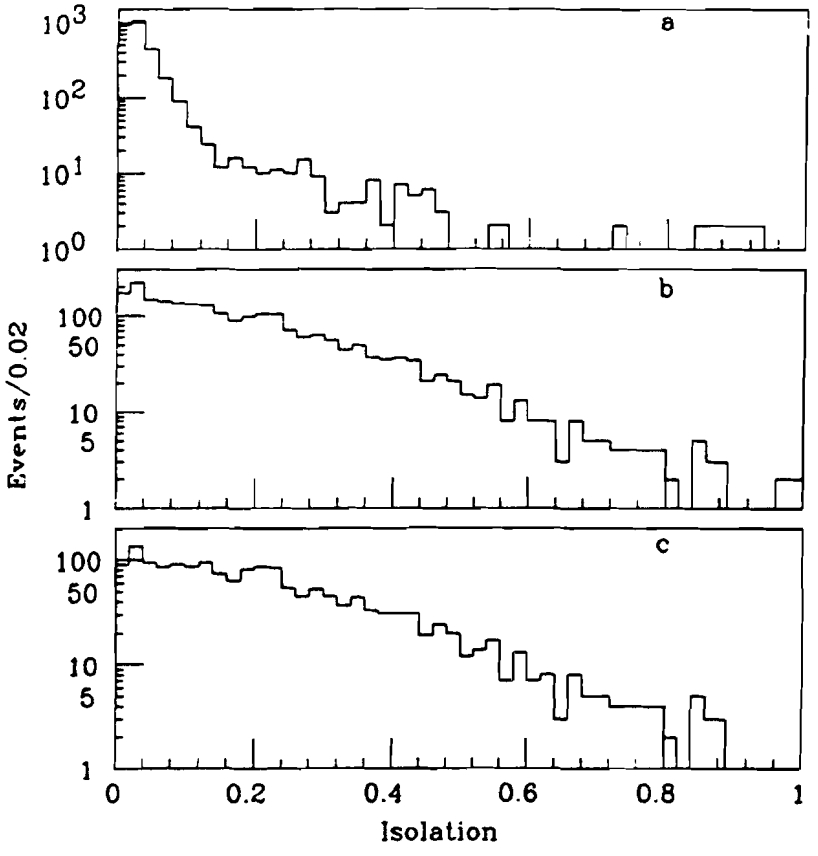

Figure 20. Isolation distributions for the samples used in estimating the W background. (a) is for the W sample, (b) is for control sample 1, and (c) is for control sample 2.

If we also include the decay $W \rightarrow \tau \rightarrow e$, we estimate a background of $0\ ^{+31}_{-0}$ events from heavy top decays into real W's.

A large background source is from the sequential decay

$$W \rightarrow \tau\,\nu, \quad \tau \rightarrow e\,\nu\,\nu,$$

where the experimental final state is identical to that from the decay $W \rightarrow e\,\nu$. The main difference is that the electron E_T and $\not{E}_T$ spectra are much softer in the $W \rightarrow \tau\,\nu$ decay. Since $W \rightarrow \tau\,\nu$ has the same branching fraction as $W \rightarrow e\,\nu$ in the Standard Model, a determination of the relative acceptance of direct decays to the sequential decays gives us the fraction of events in the sample which come from $W \rightarrow \tau\,\nu$ decays.

To estimate this background, we need to determine the ratio of the acceptances, $R(\frac{e}{\tau})$. In this ratio, we include the branching fraction of the decay $\tau \rightarrow e\,\nu\,\nu$. Using the ISAJET program to generate the process $W \rightarrow \tau\,\nu$ and $\tau \rightarrow e\,\nu\,\nu$ and the detector model discussed in section 5, we find that $R(\frac{e}{\tau}) = 27 \pm 3$. To estimate the background contribution to our sample, we need to take into account the effect of other backgrounds, since $R(\frac{e}{\tau})$ relates only the $W \rightarrow e\,\nu$ and $W \rightarrow \tau \rightarrow e$ samples.

The total number of W candidate events (W_{cand}) can be written

$$W_{cand} = (W \rightarrow e\,\nu) + (W \rightarrow \tau\,\nu) + \text{other background}, \qquad (7.2)$$

where other background is the background estimate from other processes and

$$(W \rightarrow \tau\,\nu) = \frac{(W \rightarrow e\,\nu)}{R(\frac{e}{\tau})}. \qquad (7.3)$$

Using our numbers for W_{cand} (2664 events), other background (totaling 148 ± 48), and $R(\frac{e}{\tau}) = 27 \pm 3$, we estimate the background from the sequential decay $W \rightarrow \tau \rightarrow e$ to be 90 ± 10 events.

Combining all the backgrounds, we estimate the total background in the W sample is $238\ ^{+\ 62}_{-\ 53}$ events. In combination with the W sample of 2664 events, we find the number of W candidate events to be 2426 ± 52 (stat) $^{+\ 53}_{-\ 62}$ (sys).

7.2 Z^0 Backgrounds

Backgrounds to the Z^0 sample are not as high as backgrounds in the W sample, since we ask for two high p_T, isolated electron candidates in the Z^0 selection. However, we do expect backgrounds from QCD processes and from the sequential decay $Z^0 \rightarrow \tau\ \tau$, where both τ's decay into e's. We will discuss the backgrounds in the order of the size of their contributions.

The dominant background source is from QCD processes, where partons fluctuate to look like electrons. We use the isolation of the electron candidates, in conjunction with the invariant mass of the two candidates, to estimate the contribution of this background.

We use the sample of non-isolated electrons discussed above. In the following, we refer to the central electron candidates in this sample as the first electron. We pick events which have a second electron candidate which passes all requirements outlined in section 4.6 except for the isolation requirement. The pair mass of this sample is required to be in the window 70 GeV/c^2 - 110 GeV/c^2. As can be seen in figure 21, this sample is dominated by Z^0 events. We define 4 categories of events:

- Events with first electron Iso < 0.1, second electron Iso < 0.1 (the Z^0 sample).
- Events with first electron Iso < 0.1, second electron Iso > 0.2 (the $Iso1$ sample).
- Events with first electron Iso > 0.2, second electron Iso < 0.1 (the $Iso2$ sample).
- Events with first electron Iso > 0.2, second electron Iso > 0.2 (the $NonIso$ sample).

We compute the background to the Z^0 sample as an average of three estimates.

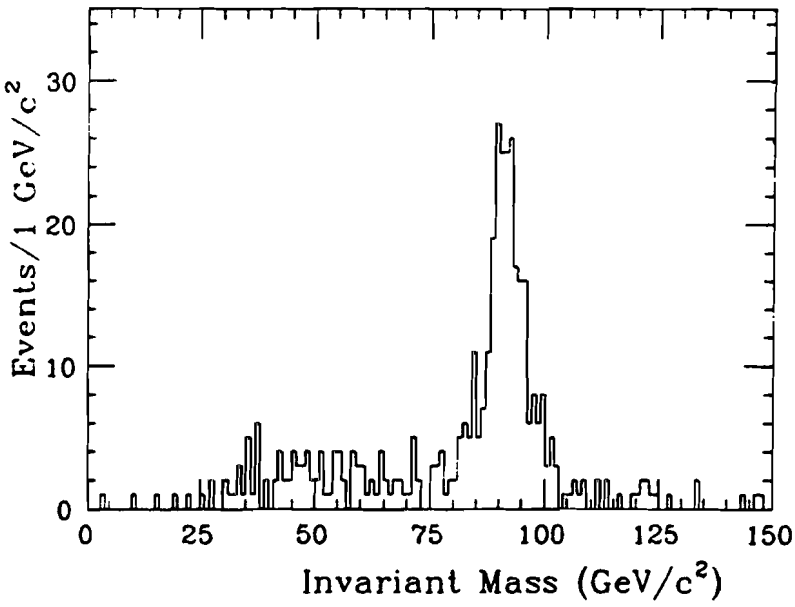

Figure 21. Invariant mass distribution for events with two electron candidates passing all but the *Iso* requirements.

The first makes use of the following equation:

$$\frac{Z^0 \text{ background}}{\#\text{ events in the } Iso1 \text{ sample}} = \frac{\#\text{ events in } Iso2 \text{ sample}}{\#\text{ events in } NonIso \text{ sample}} \tag{7.4}$$

We also use the control samples 1 and 2 used in section 7.1 for the W background and define the Z^0 background as follows:

$$\frac{Z^0 \text{ background}}{\#\ Iso > 0.3 \text{ in the } Iso2 \text{ sample}} = \frac{\#\ Iso < 0.1 \text{ in control sample 1 or 2}}{\#\ Iso > 0.3 \text{ in control sample 1 or 2}} \tag{7.5}$$

By combining these three estimates, we estimate the background in the Z^0 sample is 5 ± 3 events.

We also consider the process $Z^0 \rightarrow \tau^+\tau^-$, where both τ's look like electrons. Using ISAJET and a full detector simulation, we find no events with an invariant mass above 50 GeV/c^2 in a Monte Carlo sample corresponding to roughly twice the size of the data sample. We consider the background contribution from the process $Z^0 \rightarrow \tau^+\tau^-$ to be negligible.

The total background estimate for the Z^0 sample is 5 ± 3 events. In combination with the sample of 243 candidate events, we find the number of Z^0 candidates to be 238 ± 16 (stat) ± 3 (sys) events.

Chapter 8

Further Corrections

There are two small corrections which we need to apply to our calculation of the efficiencies described in section 6. The first applies to the central electron selection, so it is common to both the W and Z^0 samples, while the second applies only to the Z^0 sample.

8.1 Vertex Correction

In the calculation of the acceptances described in section 5, we used a Gaussian vertex distribution, with σ = 30 cm, cut at 2σ. This distribution and the cut are motivated by the vertex distribution we see in the data. Figure 22 shows the vertex distribution for events with an EM cluster with E_T > 20 GeV. Superimposed on the data is a Gaussian distribution which has a mean = 0 and σ = 30 cm, which are the default values used in the acceptance calculations. When we fit the distribution, we find a mean of -0.5 ± 0.3 and σ = 29.7 ± 0.5 cm. We now need to include the effect of the $|Z_{vert}| < 60\ cm$ cut in our calculation of the efficiency. From Gaussian statistics, we calculate the efficiency of the vertex cut to be 0.959 ± 0.005, where the error reflects the uncertainty in the fitted σ.

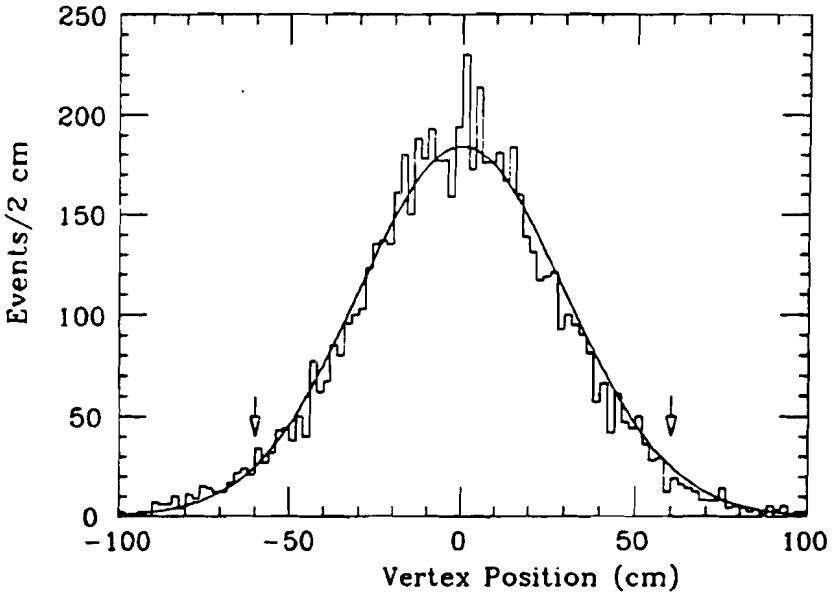

Figure 22. The vertex distribution for central electron clusters. The curve is a Gaussian with mean = 0 and σ = 30 cm.

8.2 Drell-Yan Correction

The experimental signature we use to tag the presence of Z^0 production is the presence of two high p_T, isolated electrons with an invariant mass near the Z^0 mass. The process $\bar{p}p \rightarrow \gamma^* \rightarrow e^+e^-$ has this signature as well. We measure the production of e^+e^- pairs in the mass range of 70 — 110 GeV/c^2, where we have contributions from both the γ and the Z^0. In addition, since the Z^0 has a non-zero width, there are e^+e^- events through the Z^0 resonance outside the mass range chosen. Integrating the contribution from the matrix element $|Z^0+\gamma|^2$ over the mass range 70 - 110 GeV/c^2 and the contribution from the matrix element $|Z^0|^2$ over the mass range 50 - 150 GeV/c^2, we find that the ratio of the full Z^0 contribution to the $Z^0 + \gamma$ contribution is 1.01 $\pm$ 0.01. We therefore apply a net multiplicative correction of 1.01 $\pm$ 0.01 to the e^+e^- cross section.

Chapter 9

Luminosity Measurement and Normalization

The luminosity in a collider can be measured either through direct measurement of beam parameters or from the measurement of a process with a known rate. CDF has chosen to use a combination of these methods to measure the integrated luminosity recorded during the 1988-1989 data run.

The Tevatron was run at two different energies, $\sqrt{s} = 546$ GeV and $\sqrt{s} = 1800$ GeV. The majority of running was done at the higher energy, with an integrated luminosity of ~ 4.5 pb^{-1} at $\sqrt{s} = 1800$ GeV and ~ 10 nb^{-1} at $\sqrt{s} = 546$ GeV. All the data discussed in other sections of this paper came with the Tevatron running at the higher beam energy.

We have used the interaction rate as measured in the BBCs at both energies, in conjunction with the beam parameters measured by the Fermilab Accelerator division and the $\bar{p}p$ cross sections measured by UA4 at the S$\bar{p}p$S collider at CERN [59], to calibrate our luminosity measurement. The current method does not depend heavily upon a Monte Carlo calculation since the Monte Carlo enters principally through computation of the ratio of geometric acceptance in the two experiments.

9.1 Luminosity Measurement

The Beam Beam Counters, scintillator planes located 5.8 m from the nominal interaction point, serve as the luminosity monitors for CDF. The CDF trigger system required a coincidence of hits in the east and west BBCs. By monitoring the rate of hits in these counters, we have a process to which we can normalize all other cross section measurements. To get an absolute normalization of the BBC cross section (σ_{BBC}), we use the rate seen in these counters and the luminosity measured with beam parameters. In previous work, CDF has used $\sigma_{BBC}^{nom} = 44 \pm 6.6$ mb [55].

The transverse profile of the beam is measured with flying wires – wires moved through the beam [60]. A wall current monitor measures bunch intensities and the longitudinal profile [61]. The luminosity at CDF is calculated with these parameters and knowledge of the accelerator lattice function. Uncertainties in this calculation come from measurement errors, calibration uncertainty, and uncertainties in the lattice function. The overall uncertainty is estimated to be 10% [62]. This uncertainty is energy independent.

At both $\sqrt{s} = 546$ GeV and $\sqrt{s} = 1800$ GeV, we measure the beam parameters and the rate in the BBCs. We are then able to measure how σ_{BBC} changes with $\sqrt{s}$, via the ratio of the accelerator luminosity calculated from beam parameters. This ratio has a systematic uncertainty free from the overall normalization uncertainty. By normalizing at $\sqrt{s} = 546$ GeV, where previous measurements with similar geometry have been made, we can measure the effective cross section seen by the BBCs at $\sqrt{s} = 1800$ GeV and extract the integrated luminosity recorded.

9.2 Normalization

We have selected a series of accelerator fills where the data are internally consistent. Many of the variables that we are interested in have to be reconstructed from other measurements (e.g. horizontal and vertical emittances of the beam).

To do this reconstruction accurately required an understanding of the accelerator conditions and programs at the time the data were taken [63]. This selection is independent of conditions at CDF.

In figure 23, we show a distribution of the rate as measured with the BBCs (R_{BBC}) compared to the luminosity as measured with accelerator parameters (L_{acc}) for both $\sqrt{s}$ = 1800 GeV and $\sqrt{s}$ = 546 GeV. We then use the relation

$$\frac{\sigma_{BBC}^{1800}}{\sigma_{BBC}^{546}} = \frac{R_{BBC}(1800)}{R_{BBC}(546)} \frac{L_{acc}(546)}{L_{acc}(1800)} \tag{9.1}$$

to extrapolate the σ_{BBC} from 546 GeV to 1800 GeV. The ratio $\frac{R_{BBC}}{L_{acc}}$ at 1800 GeV has been corrected by -3 ± 2% for dynamic beam–beam interaction effects, which change the focus properties at the interaction region [64]. These effects predict a linear dependence of the ratio with L, which is seen in the data (figure 24).

We use two methods to calculate σ_{BBC}^{546}. The first is to use the luminosity as calculated from beam parameters and the accelerator lattice. This method gives an effective beam beam counter cross section of 32.8 ± 3.6 mb. The second method is to use values reported by the UA4 collaboration.

The UA4 experiment used trigger counters similar in geometry to the BBCs used by CDF. From their measurements of ρ, σ_{el}, and σ_{tot}, and the double arm fraction (f_{DA}) [65] of the UA4 trigger counters [59], we define

$$\sigma_{UA4}^{obs} = (1 - \frac{\sigma_{el}}{\sigma_{tot}}) \cdot \sigma_{tot} \cdot f_{DA}. \tag{9.2}$$

We calculate σ_{UA4}^{obs} = 38.9 ± 1.8 mb [66]. Using the MBR Monte Carlo [67], we then calculate the relative acceptance of the CDF BBCs in comparison to the UA4 trigger counters. This correction is necessary since the UA4 trigger counters cover a different geometric area ($3.0 < |\eta| < 5.6$) then the BBCs. The correction due to different η coverage is -2.5 ± 2.5%. We also correct for the inefficiencies in the BBCs due to radiation damage suffered during the course of the data taking. Radiation damage and its effects at 1800 GeV are measured from data triggered solely on beam

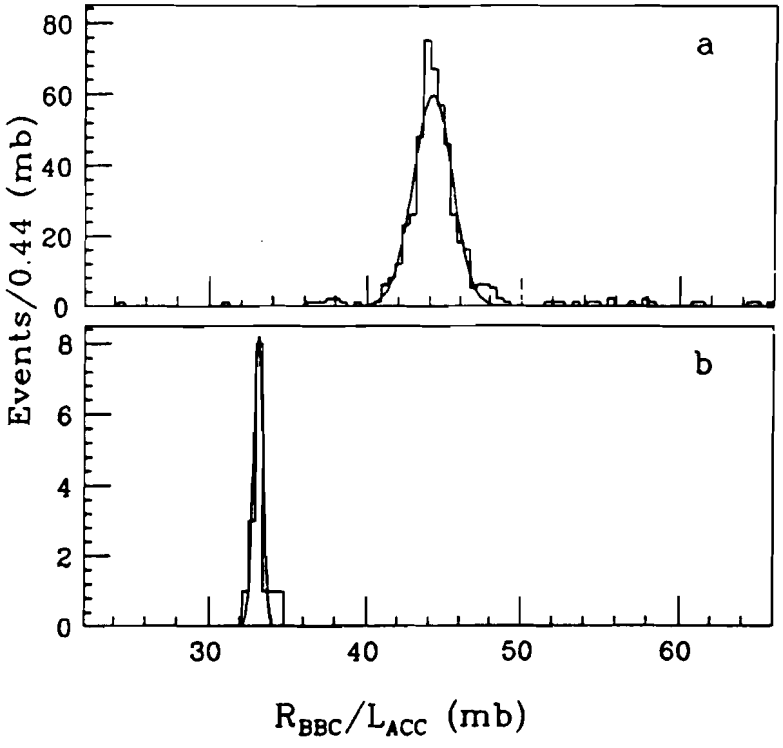

Figure 23. Distributions of $\frac{R_{BBC}}{L_{acc}}$. The data for $\sqrt{s} = 1800$ GeV is in (a), with a fitted Gaussian with $\bar{x} = 44.16$ and $\sigma = 1.28$ superimposed. The data for $\sqrt{s} = 1800$ GeV is in (b), with a fitted Gaussian with $\bar{x} = 33.17$ and $\sigma = 0.30$ superimposed

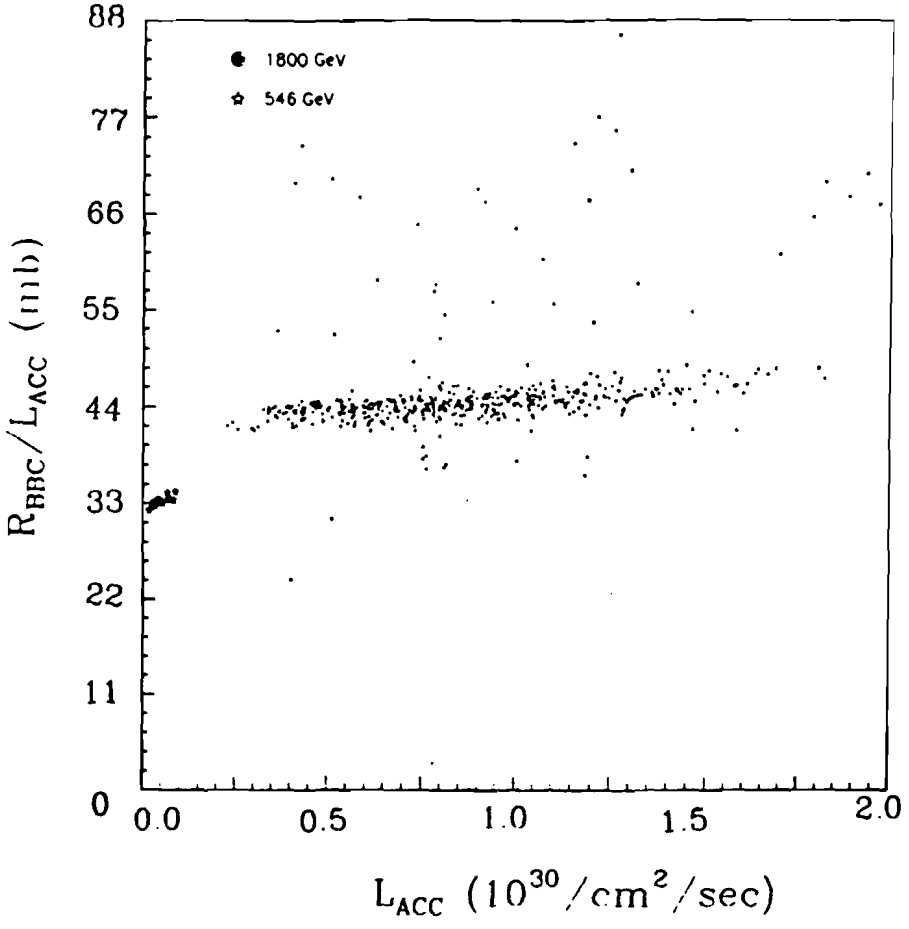

Figure 24. The ratio $\frac{R_{BBC}}{L_{acc}}$ as a function of the instantaneous luminosity. Data from accelerator fills with $\sqrt{s} = 546$ GeV and $\sqrt{s} = 1800$ GeV are plotted, with the 546 GeV data the clump at the lower left.

crossings. The magnitude of this correction at 1800 GeV is -0.7%. This inefficiency is extrapolated to 546 GeV using the MBR Monte Carlo, giving an inefficiency of 2.2 ± 2.2%. The value for σ_{BBC}^{546} from this method is 37.1 ± 2.1 mb.

To derive the final value of σ_{BBC}^{546}, we average the measurements from the accelerator calculation and the UA4 normalization weighted by their respective errors. In summary, $\sigma_{BBC}^{546} = 36.0 \pm 1.8$ mb, where the answer is dominated by the UA4 normalization. We calculate $\sigma_{BBC}^{1800} = 46.8 \pm 3.2$ mb. We wish to stress that this normalization is not a physical cross section, but a visible cross section not directly related to underlying physics models. This method depends upon the similarity of the CDF luminosity monitors to the UA4 counters and the ability to use the information from the accelerator measurement of the luminosity.

9.3 Cross Checks

As the instantaneous luminosity grows, the rate of bunch crossings with multiple interactions also grows. Using Poisson statistics, we can estimate the probability of having 2 or 3 interactions in a bunch crossing. We find that the ratio of the probability of having 2 interactions to the probability of having 1 interaction is predicted to be $1.75 \times 10^{-6} \times R_{BBC}$, where R_{BBC} is the rate in the BBCs in Hertz (this number is directly related to the 3.5 μsec between beam crossings). We use this prediction to make a correction (on the order of 9% at 50 kHz) to the measured rate in the BBCs to account for multiple interactions.

The ratio of the number of events with two vertices to those with one vertex as a function of the rate in the BBCs is a check on the BBC cross section. To do this properly, we must first correct for inefficiencies in vertex finding. The CDF vertex finding algorithm has inefficiencies in resolving multiple vertices if the separation of the vertices in Z is too small. We calculate the efficiency for finding secondary vertices using the distribution of two vertex separation from multiple vertex events

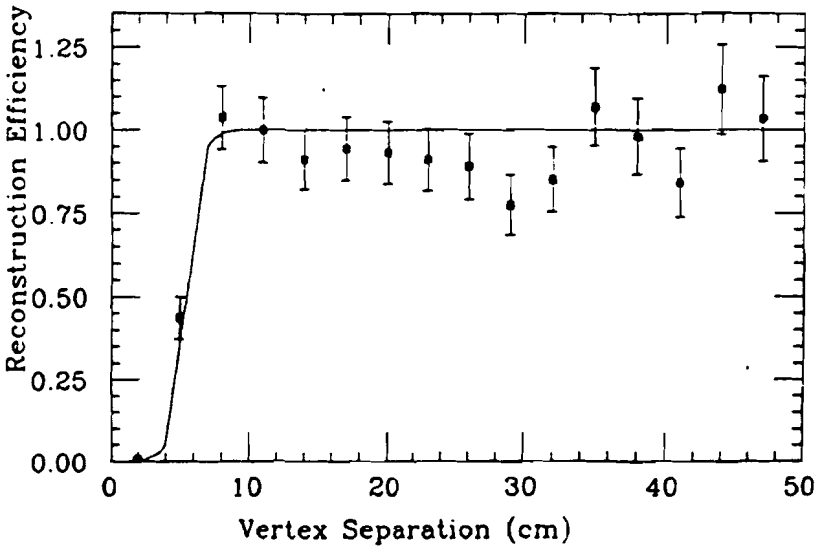

Figure 25. The secondary vertex finding efficiency as a function of vertex separation.

in the inclusive central electron sample (described in section 4.6), including the assumption that the vertex distribution is Gaussian with $\sigma = 30$ cm. Figure 25 shows the efficiency as a function of the vertex separation.

Figure 26 shows the ratio of the number of events with 2 vertices to those with 1 vertex as a function of the R_{BBC}. The number of 2 vertex events has been corrected for the inefficiency in finding a second vertex. A linear fit gives a slope of $(1.91 \pm 0.08) \times 10^{-6}$, within 2σ of the predicted value of 1.75×10^{-6}.

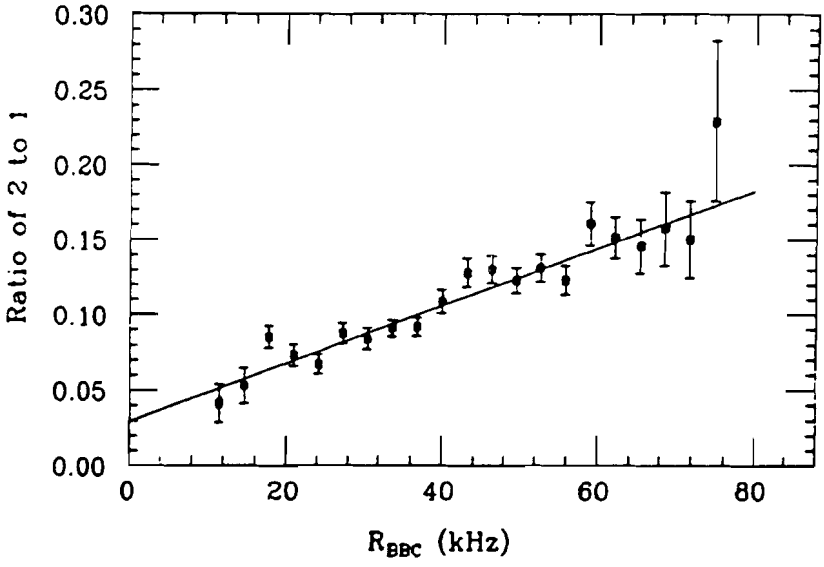

Figure 26. The ratio of events with 2 vertices to events with 1 vertex as a function of R_{BBC}. The number of events with 2 vertices has been corrected for vertex finding inefficiencies.

Chapter 10

Results and Conclusions

10.1 Cross Sections

The expression for the cross section takes into account the background, efficiencies, acceptances, and integrated luminosity through the following formula

$$\sigma(W \rightarrow e\,\nu) = \frac{\text{Candidates} - \text{Background}}{\int Ldt \cdot \epsilon \cdot A} \tag{10.1}$$

where ϵ is the selection efficiency and A is the acceptance. For the measurement of $\sigma(W \rightarrow e\,\nu)$ and $\sigma(Z^0 \rightarrow e^+e^-)$, the number of candidates, backgrounds, efficiencies, and acceptances are summarized in table 12. A straightforward application of equation 10.1 leads to the following results.

The final cross section for W production and subsequent decay to electron and neutrino is $\sigma(W \rightarrow e\,\nu) = 2.19 \pm 0.04$ (stat) $\pm$ 0.21 (sys) nb, where the systematic uncertainty reflects the uncertainty in our knowledge of the background subtraction, acceptance and efficiency corrections, and luminosity normalization. The dominant systematic uncertainty in the determination of $\sigma(W \rightarrow e\,\nu)$ is the 6.8% error in the luminosity normalization. The final cross section for Z^0 production and subsequent decay into electrons is $\sigma(Z^0 \rightarrow e^+e^-) = 0.209 \pm 0.013$ (stat) $\pm$ 0.017 (sys) nb, where the luminosity normalization uncertainty dominates the systematic uncertainty.

Figure 27 shows a comparison of the CDF measured values for $\sigma(W \rightarrow e\,\nu)$ and $\sigma(Z^0 \rightarrow e^+e^-)$ to theoretical predictions [68]. Included on this plot are recent values for $\sigma(W \rightarrow e\,\nu)$ and $\sigma(Z^0 \rightarrow e^+e^-)$ at $\sqrt{s} = 630$ GeV from the UA2 collaboration [69]. The theoretical predictions used $M_W = 80$ GeV/c^2 and $M_Z = 91.1$ GeV/c^2 and assumed that the decay channels into top were closed.

In a previous publication [17], a different assumption on the W branching ratio into electrons (we assumed a top mass of 45 GeV/c^2) was made. This assumption affected the theoretical prediction more than the experimental measurement, since the top mass affects the branching ratio into electrons. Recent measurements by CDF [43, 54] and UA2 [70] on these two quantities have helped reduce theoretical uncertainties in the prediction of the cross section times branching ratio. The changed assumptions both increase the predicted cross section, bringing it closer into agreement with previously measured values. The current theoretical predictions agree quite well with the most recent experimental measurements at both $\sqrt{s} = 630$ GeV and $\sqrt{s} = 1800$ GeV.

10.2 The ratio $R = \sigma(W \rightarrow e\,\nu)\ /\ \sigma(Z^0 \rightarrow e^+e^-)$ and the W width

The ratio, R, of $\sigma(W \rightarrow e\,\nu)$ to $\sigma(Z^0 \rightarrow e^+e^-)$ and the individual cross sections themselves are interdependent quantities. From the perspective of experimental measurement, they can be considered as three separate quantities. In a previous publication [18], CDF has documented a measurement of $R = 10.2 \pm 0.8$ (stat) $\pm$ 0.4 (sys). In this measurement, we applied selection criteria designed to minimize the systematic uncertainties in the ratio.

In order to lower backgrounds and minimize systematic uncertainties, events with energy clusters other than the electrons from W and Z^0 decays were rejected in the analysis. Such a requirement is fine in measuring the cross section ratio,

where the numerator and denominator are affected almost equally, but not for the independent measurements of the numerator and the denominator.

Allowing for the presence of energetic clusters in addition to identified electrons has increased the size of the W and Z^0 datasets (thus decreasing the statistical error) but has also increased the levels of background in the samples. Uncertainty in the level of the background also increases significantly. Taking the individual cross sections reported in section 10.1 and taking into account the correlated errors in the two measurement we find a value of $R = 10.5 \pm 0.7$ (stat) $\pm$ 0.6 (sys). Due to the increased systematic error in this method, we believe that the measurement documented in reference [18] contains our best knowledge of the ratio of the cross sections.

The ratio, R, can be expressed as [71]

$$R = \frac{\sigma(W \rightarrow e\nu)}{\sigma(Z^0 \rightarrow e^+e^-)} = \frac{\sigma(\bar{p}p \rightarrow WX)}{\sigma(\bar{p}p \rightarrow Z^0X)} \frac{\Gamma(W \rightarrow e\nu)}{\Gamma(Z^0 \rightarrow e^+e^-)} \frac{\Gamma(Z^0)}{\Gamma(W)}. \qquad (10.2)$$

From R, either the ratio of total widths $\Gamma(Z^0)/\Gamma(W)$ or the branching ratio for W into electrons can be extracted with the knowledge of the ratio of production cross sections [72], the partial and total widths of the Z^0, and the partial widths of the W .

Using our value for $R = 10.2 \pm 0.8$ (stat) $\pm$ 0.4 (sys), predicted values of production cross section ratio $\sigma(\bar{p}p \rightarrow WX)/\sigma(\bar{p}p \rightarrow Z^0X) = 3.23 \pm 0.03$ [72], measured values of $\Gamma(Z^0) = 2.496 \pm 0.016$ GeV [73], $\sin^2\theta_W = 0.229 \pm 0.007$ [52], and $\Gamma(W \rightarrow e\nu)/\Gamma(Z^0 \rightarrow e^+e^-) = 2.70 \pm 0.02$ [74], we extract $\Gamma(W) = 2.12 \pm 0.20$. The standard model prediction with $M_W = 80.0$ GeV/c^2, $\alpha_s = 0.13$, and $M_{top} > M_W - M_b$ is $\Gamma(W) = 2.07$ GeV. This value for $\Gamma(W)$ has changed since reference [18] due to new measurements of $\Gamma(Z^0)$.

Recent searches have set lower limits on M_{top} up to 89 GeV/c^2 assuming standard-model decays [57, 54] and up to 45 GeV/c^2 independent of decay mode [73]. Figure 28 shows a prediction for the ratio $\Gamma(W)/\Gamma(W \rightarrow e\nu)$as a function of the top

mass. From the values quoted above and $\Gamma(Z^0 \rightarrow e^+e^-) = 83.7 \pm 0.07$ MeV [73], we find that $\Gamma(W)/\Gamma(W \rightarrow e\nu) = 9.47 \pm 0.86$. This value excludes M_{top} below 49 (44) GeV/c^2 at the 90% (95%) confidence level independent of the decay modes of the top quark [75]. We use this ratio since it depends only weakly on the W mass. Again, the limit has improved due to new measurements of $\Gamma(Z^0)$ and $\Gamma(Z^0 \rightarrow e^+e^-)$.

Combining knowledge of the proton structure functions, W and Z^0 couplings, and QCD corrections leads to predictions of the cross section for production and decay of W and Z^0 bosons in $\bar{p}p$ collisions. We have shown that the predictions are consistent with experimentally measured quantities. Oscar Klein's W boson has become a good and well understood friend.

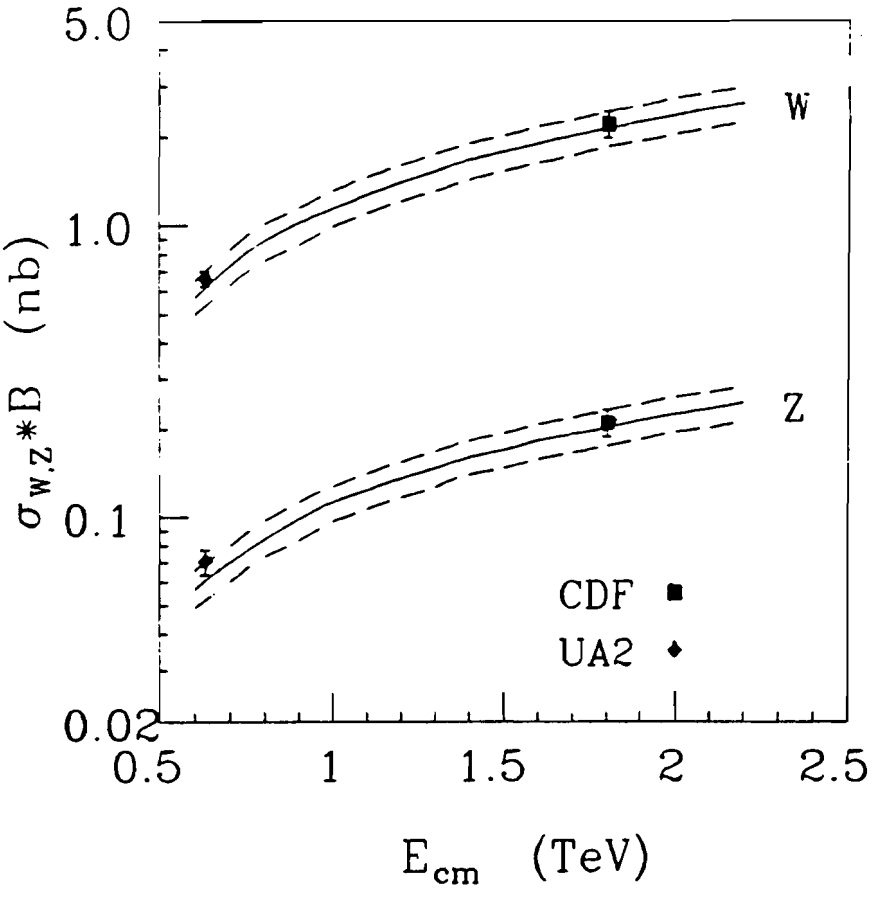

Figure 27. Comparison of experimental measurements with theoretical predictions [68]. The dashed lines indicate the 1σ error limits for the theoretical curve. Recent measurements by the UA2 collaboration are also plotted [69].

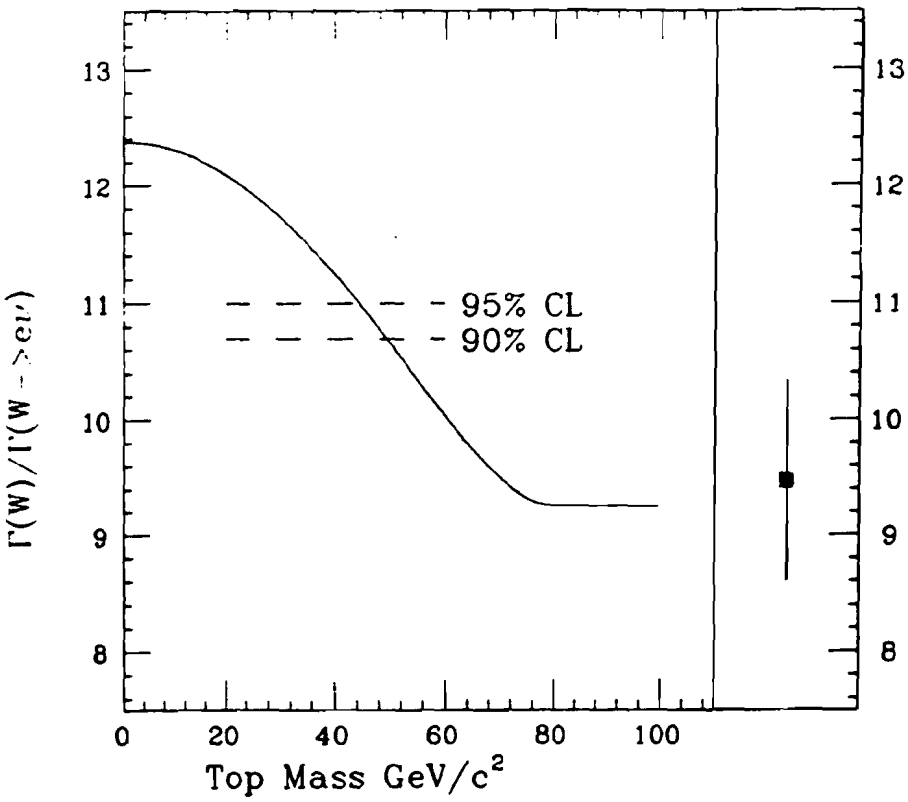

Figure 28. The predicted value for $\Gamma(W)/\Gamma(W \rightarrow e\,\nu)$ as a function of the top-quark mass for M_W = 80.0 GeV/c^2 and α_s =0.13. The value calculated from equation 10.2 with 90% and 95% - C.L. limits is shown. We use this ratio since it depends only weakly on the W mass.

Table 12. Summary of results

	W Events	Z Events
Candidates	2664	243
Background		
QCD	100 ± 50	5 ± 3
$W \rightarrow \tau\,\nu$	90 ± 10	-
$Z^0 \rightarrow e^+e^-$	40 ± 15	-
$Z^0 \rightarrow \tau^+\tau^-$	8 ± 4	< 0.5
top	$0 + 31 - 0$	-
Total	$238 + 62 - 53$	5 ± 3
Signal	$2426 \pm 52 + 53 - 62$	$238 \pm 16 \pm 3$
Acceptance	0.352 ± 0.015	0.371 ± 0.007
F_{cc}	-	0.40
F_{cp}	-	0.47
F_{cf}	-	0.13
c_1	0.84 ± 0.03	0.84 ± 0.03
c_2	-	0.93 ± 0.03
p	-	0.91 ± 0.03
f	-	0.91 ± 0.04
ϵ_ν	0.96 ± 0.02	-
ϵ_W, ϵ_Z	0.81 ± 0.04	0.80 ± 0.03
Drell-Yan Correction	-	1.01 ± 0.01
Z-vertex Efficiency	0.959 ± 0.005	0.959 ± 0.005
Luminosity	4.05 ± 0.28 pb^{-1}	4.05 ± 0.28 pb^{-1}
Cross Sections	$2.19 \pm 0.04 \pm 0.21$ nb	$0.209 \pm 0.013 \pm 0.017$ nb

Appendix A

List of Supporting Documents

This appendix lists supporting documents for the work done in the text. Most of these documents were written as internal documentation for the CDF collaboration and should be treated as such. Contact Carol Picciolo to obtain copies of these documents. Included below are the CDF note number, the authors, the title, and a short description of the contents. Many of the details of the event reconstruction, analysis, and work can be found in these documents (they are listed in increasing numerical order, not in order of importance).

- **CDF649** R.G. Wagner *Simulation of Radiative W Decay: An Interim Status Report*

  Bob's work concentrated on writing and implementing into the CDF Monte Carlo system a generator for radiative W decay. It became instrumental in the work of setting the CEM energy scale.

- **CDF744** C. Campagnari, C. Grosso-Pilcher *Trigger vs. MX studies*

  This note, by UCHEP members Claudio and Carla, documents the trigger energy response vs. the data acquisition system energy response. Since the two systems used different electronics to sample the detector response, it was necessary to study the comparative level of response. The main application to this work of these studies concerned the response of the CEM. They found that the energy in the trigger was $\sim$ 97% of the energy as read out by the data acquisition system. Since we used a threshold of 20 GeV in the analysis and the trigger threshold was 12 GeV, this analysis is not effected by the different response.

- **CDF775** R.G. Wagner *Summary of Results on Radiative W Decay*

  This note contains additional documentation on Radiative W Monte Carlos and was the final source used for further studies.

- **CDF794** C. Campagnari, M. Campbell, P. Tipton *Running Production on the Spin Output*

Claudio, Myron, and Paul organized a data stream to run the offline production package on the output from the Spin Cycle. They ran the analysis on the computing facilities at the University of Chicago. The first public results from CDF in 1989 came with data from this effort.

- **CDF795** P. Tipton, J.J. Schmidt, B. Winer *A summary of the New Spin Cycle*

  Paul, JJ, Brian, Claudio, and myself set up the Spin Cycle executable and babysat the running of the stream. This document summarizes what went into the data selection for the spin cycle.

- **CDF799** Y. Hayashide, et al., *Response Maps of the CDF Endplug Electromagnetic Calorimeter*

  One correction factor applied to the energy of candidate clusters in the PEM was a response map. The analysis used to derive this map is documented in this note.

- **CDF802** D. Amidei *The ElectroWeak Filter*

  The ElectroWeak Filter was written by Dan and myself, with much input and aid from other members of the collaboration. It was a filter which ran in the production stream, designed to select events which had characteristics of Electroweak Physics. Almost all the analysis described in this thesis used data which passed this filter. This note documents the selection criteria necessary for events to pass the Electroweak Filter.

- **CDF806** D. Baden, A. Clark, G.P. Yeh *Mini and Micro DSTs*

  Mini and Micro DSTs are condensed versions of the DSTs (Data Summary Tapes). The DSTs contained both the raw data and reconstructed data in all its glorious detail. The Minis and Micros contained smaller versions of the same, either in condensed versions of the raw data (Mini) or just the reconstructed data (Micro).

- **CDF832** L. Nodulman, W. Trischuk *Missing* E_T *Data Sets 1988*
  The $\not\!\!E_T$ dataset described in the efficiency section and used to measure the electron selection efficiencies came from the Missing E_T streams. This note documents the requirements for an event to be in this stream.

- **CDF841** M. Binkley, J. Hinkelman *Road Searching Routines for the VTPC*
  Electron candidates in the plug were required to have a certain fraction of hits along a road in the VTPC. This note documents what goes into defining that road.

- **CDF860** J. Proudfoot *Pre-Installation Validation of Level 3 Filter CEPFLT*
  The electron trigger existed at three levels, with the requirements at level 3 a subset of the offline analysis requirements. This note documents the checks made to ensure that the code was working as expected in the level 3 system (since it was impossible to do online debugging of this system).

- **CDF869** T. Kamon, S. Kim *Electron Energy Correction in PEM Dead Layers*
  More information on how we defined electron energy for the PEM calorimeter. The PEM consists of 34 layers of gas proportional tubes, interleaved with lead radiator. Several of these layers (in various locations) are known to be dead, while the calorimeter was calibrated with all layers working. The algorithm to correct the energy for dead layers is explained in this note.

- **CDF883** W. Trischuk, et al., *A Determination of the Absolute Calibration of the CEM Energy Scale*
  We based our electron selection on 20 GeV electrons in the central rapidity region. To fully understand this selection in terms of kinematical acceptance, we need to understand the energy scale of the CEM. This note describes the method to take the scale from the test beam calibration and convert it to a better scale.

- **CDF892** T. Kamon, S. Kim *Electron Energy Correction in PEM Dead Layers*

(II)

This note continues in the footsteps of **CDF869**, describing how the correction for dead layers in the PEM calorimeter was implemented.

- **CDF905** T. Kamon *CEMMAP Description — CEM Response Map Correction —*

  The normalization of the CEM scale in the test beam was to the center point of the calorimeter face — electrons of the same energy which did not hit in this point gave different response. The wedges were scanned in the test beam and a response map devised. This note documents how to use the response map.

- **CDF906** S. Kim, Y. Morita, Y. Fukui, S. Ogawa, T. Kamon *Electron Energy Correction with PEM Response Map and Quadrant Gain Factors*

  In addition to the response maps devised for the PEM, corrections were made for the different response in each quadrant. Only one quadrant was directly calibrated in the test beam — the other 7 quadrants were assumed to have the same response. From studies of transverse mass distributions for W's invariant mass distribution for Z^0's, the relative response of each the 7 quadrants not calibrated in the test beam was set to be the same as the one that was in the test beam. This note is the first of a series in this study.

- **CDF922** C. Campagnari, P. Derwent, P. Tipton, B. Winer *A Search for Heavy Top in the Inclusive W sample*

  Claudio, Paul, Brian, and myself took our inclusive W sample and looked for the presence of additional W + jet events. It was our first attempt at understanding acceptance, efficiencies, and backgrounds for the W sample. The selection criteria for W's has changed somewhat since this note, but the general approach is still being used.

- **CDF932** R.J. Hollebeek, K.J. Ragan, P.K. Sinervo, J. Walsh, H.H. Williams

Comparison of E + Jets with W + Jets Monte Carlo

The group at Penn was also pursuing top, though they were looking at a lower mass range than the group above. This note documents how well the W + jets Monte Carlo duplicated what was seen in the data. It is included here because I used a similar Monte Carlo for my study of $\not\!\!E_T$ efficiency.

- **CDF933** J. Proudfoot, F. Ukegawa, B. Wicklund *Central Strip Chamber Alignment*

  One selection criteria used for electrons is how well the extrapolated track position matches the strip cluster position. Jimmy, Fumi, and Barry did a lot of work studying the location of the strip chambers in the wedges. This note documents the small offsets and shifts that they discovered (through investigating with the data — it's marvelous what one can do with a rich dataset).

- **CDF935** J. Proudfoot *Electron Identification in the CDF Central Calorimeter*

  I am indebted to this note, which is a writeup of a talk Jimmy gave at a workshop for SSC calorimetry, because in it I found the definition of *Lshr*. For all future CDFers, keep this in mind.

- **CDF948** L. Nodulman, W. Trischuk *1988-89 Missing* E_T *Resolution*

  The $\not\!\!E_T$ resolution is an essential part of understanding the efficiency of the $\not\!\!E_T$ requirement in the event selection. While I did not do the work, others made sure that the simulation was able to duplicate the $\not\!\!E_T$ resolution seen in data. I thank them for it.

- **CDF955** D. Baden, et al., *The V5.1 CDF Production Package*

  If you want to know exactly what went into the offline production package, this is the place to look. It documents the changes implemented for this production pass, the executable, command files, and data stream definitions. It was a really nice thing to have around for reference.

- **CDF960** D. Baden *The CDF Calorimetry Module - 1988/1989 Run*

Drew explains everything you want to know about the **Calorimetry** module that was used in the offline production package. This module computes tower energies based on the raw data, so it is at the heart of all analysis based on energy selection (as our electron selection is). If you want to know what went into the energy definition for your data, you should read this note.

- **CDF966** J. Hauser *A Guide to the Triggers used in the 1988-1989 CDF Data Run*

  Jay did the collaboration a service with this note, which documents which triggers went with which tables and how many data tapes were taken with each table. Every trigger used during the course of the run for physics data is documented in this note.

- **CDF968** J.S.T. Ng *Gas Calorimeter Energy Scale Cross Calibration Using Texas Towers*

  One important calibration that we use is to set the relative energy scales in the FEM calorimeter. By studying the rate of Texas towers (neutron induced pulses in the gas calorimeters) as a function of azimuth and η, Johnny was able to set relative scales for the FEM calorimeter. Many people do not realize that this correction is included in the standard CDF electron energy corrections, but it is.

- **CDF1021** S. Kim, S. Ogawa *PEM Quadrant Gain Factors*

  This note continues the work begun in **CDF905**. The main difference between the numbers reported from here and the numbers reported in **CDF905** is that the sample size increased so the statistical power increased.

- **CDF1025** C. Campagnari *A Fast W and Z Monte Carlo*

  Claudio saved all of us a lot of work by writing his own simple Monte Carlo generator for W and Z^0 events. It does not include any underlying event

information and it is not fully implemented into the CDF Monte Carlo package, but it provides a fast and easily understood generator for acceptance studies.

- **CDF1026** C. Bowers, et al. *A Measurement of the Ratio of W and Z Cross Sections*

  This note is very important. It documents the studies done in the measurement of the ratio of the W and Z^0 cross sections. Many of the methods used in this thesis are extensions of the methods first used in measuring the cross section ratio. It contains detailed documentation of how we did just about everything.

- **CDF1031** S. White *Reducing Luminosity Uncertainties*

  Sebastian took a novel approach to reducing the uncertainty in the integrated luminosity. He normalized the measurement of the luminosity by the BBCs to that measured by the accelerator division, both at $\sqrt{s}$ = 1800 GeV and 546 GeV. In doing so, he was able to bypass the extrapolations of the measured cross sections at $\sqrt{s}$ = 546 to $\sqrt{s}$ = 1800 and there related uncertainties.

- **CDF1037** P. Derwent *Electron Energy Corrections: Where They are Made and What They Are*

  Henry persuaded me to do a little digging and find out all the corrections that are made to set the energy scales for the various electromagnetic calorimeters. I learned quite a bit about the algorithms and the corrections in this search. This note contains what I learned on this subject. Some of it has changed since then, but it is still fairly up–to–date.

- **CDF1077** E. Kearns *Adjusting the FEM Energy Scale Using Z0 Events*

  Ed spent some time to adjust the scale for the FEM. It was calibrated in the test beam, but the energies it was seeing were higher than were present in the test beam. They were high enough so that the response was no longer linear — this note documents the non-linearity corrections Ed devised so that the Z^0 mass using FEM electrons was the same as from CEM electrons.

- **CDF1081** S. Errede, W. Trischuk *E/p Calibration of the CEM Calorimeter*
  The second step along the line of understanding the corrections to the CEM energy scale. It followed in the footsteps of **CDF883**, but with more Monte Carlo statistics for the radiative Monte Carlo. The numbers reported in this document were those used for the final analysis.

- **CDF1086** M. Miller *Fiducial Cuts for Electrons*
  Marsh explains the accepted fiducial regions for electrons in the 1988-89 dataset. They mainly cut away from detector cracks and boundaries, where the response to electrons is not as well known.

- **CDF1107** C. Campagnari, et al., *Measurement of Sigma(W→enu) and Sigma(Z→ee) in $\bar{p}p$ collisions*
  This note was our preliminary measurement of the W and Z^0 cross sections. It used the same selection criteria as the R measurement (**CDF1026**), except that we did not reject events with jets. The methods and results are astonishingly similar to those documented in this thesis.

- **CDF1166** M. Miller, et al., *A Standard Data Sample for W and Z analysis*
  We got together with many other people who were working on W and Z^0 physics and came up with a standard data sample. Brian, Aesook, and I put it together (with aid from the ever helpful JJ) and made it publicly available in CDF$W_Z_DATA:[ANA]. As it turned out, not everyone used this sample.

- **CDF1202** C. Grosso-Pilcher, S. White *CDF Luminosity Calibration*
  Carla and Sebastian continued the work of **CDF1031**, investigating many possible systematic effects and working to understand the accelerator division data. This note documents their work in much detail — the luminosity section of this thesis is deeply indebted to this document.

- **CDF1226** M. Binkley, S. Errede, B. Wicklund *E/p Calibration of the CEM Energy Scale*

Can you believe even more work on getting the CEM energy scale right? It has much more signigicant impact on the W and Z^0 mass analysis, but we did include corrections in our event selection. However, since we made our data sample in April and this note came out in July, we used a different scale than what is documented here. We used the numbers from **CDF1081**, which differed by 0.2% from the final number reported here.

- **CDF1254** C. Campagnari, P. Derwent, M. Miller *Checks for the W and Z Cross Section Measurement*

  One last document from the guys at Chicago concerning the W and Z^0 cross sections. The information in this note duplicates much of what is in this thesis, except that it is written for the CDF cognoscenti.

Appendix B

B0 Information

This appendix contains somewhat random documentation on things that I have worked on at B0. It contains sections on Charge Injection, LUMMON, and the trigger name database. These projects were things I worked on during my years as a graduate student and this thesis is a good place to document. For all CDF graduate students (and Chicago students in particular), this appendix is a good place to look for information on these subjects.

B.1 Charge Injection

Charge injection serves as a tool to check the electronic response of the trigger fastout circuitry in RABBIT. It makes use of the calibration circuits built onto the PM and CARROT cards to put a certain amount of charge at the front end. By careful calculation, one can trace what the magnitude of the charge should then be at the input to the trigger RAW boards. Since the program makes use of information in the RABBIT database, changes in the location of cards are transparent to the user (assuming that the RABBIT database is updated properly). Because of this feature, the future changes of CARROT to GPA should not adversely affect the performance of the code.

B.1.1 Simple Code Details

Code Location The code exists in the directory TRIGGER$CHARGE (at this writing, the logical points to usr$root2:[trigger.charge] on the B0 VAX cluster). All of the code has been compiled and placed in the object library CHARGE.OLB. There also exist .COM files to compile/link all the necessary code (COMPILE_CHARGE.COM and LINK_CHARGE.COM). The .COM files for linking have undergone much fine-tuning to get the order of object libraries right. Adjust this order at your own risk (given all the changes at B0, it may be necessary!).

Code Implementation and Structure The Charge Injection program is designed to work in units of the trigger calorimeter setup. It therefore concentrates on RAW/CAS crates as its main differentiating factor. The user selects a RAW/CAS crate and the code figures out which MX's and RABBIT crates are associated with the trigger channels. Since the program does talk to RABBIT crates, it makes use of the RESOURCE_MANAGER to ensure that it is the only process with the rights to talk to particular crates. Within a RAW/CAS crate, the user can inject charge to individual channels, scan all channels, scan η and ϕ slices, histogram the results, and do comparisons to the data acquisition readout.

The code reports back to the user the number of CRATE SUM counts for particular channels. The CRATE SUM DAC is a 10 bit DAC, with each count equivalent to 125 MeV. The output from the Charge Injection program is shifted by 2 bits, making each count 500 MeV. This assumes two things: that 1 V at the input to RAW is equivalent to 100 GeV for the central calorimeter and that 1 V is equivalent to 50 GeV for all the gas calorimeters. All of the calculations to normalize the different gains are taken care of in the code.

The main body of the code resides in CHARGE.FOR. In this file we setup the necessary RABBIT, FASTBUS, and MX information for the

B.2 LUMMON

LUMMON is a simple, straightforward, easily understood program designed to display information about trigger rates. It runs as a real time monitoring program in the B0 control room, making use of UIPACK viewports to update information as it changes. It is flexible enough to quickly add additional information to its displays.

B.2.1 Code Location

The code for LUMMON exists in the CMS library TRIGMON$CMS. At the end of the data run, there were four people with the right process rights identifiers to write to this CMS library (Aaron Roodman, Jay Hauser, Tony Liss, and myself). Contact the B0 system manager to get the proper privileges.

The code was kept in the directory TRIGMON$SCALERS. There are two modules which run in the Analysis_Control path – LUMBBC and LUMMON – which calculate the integrated luminosity from the BBC scaler information and the various trigger rates and display them. The module LUMBBC is the same as in the offline calculation of luminosity (with code in C$TRS). The module LUMMON handles the calculation of the rates, deadtimes, cross sections, and manipulates the display.

B.2.2 Program Structure

LUMMON makes use of UIPACK viewports to display and update information. Viewports make use of VAX Screen Management routines to write to particular locations on the screen. A basic structure for each viewport window is defined from a data file and the rate information is then written into locations in the viewport.

In the Analysis_Control initialization routine, the file SCALER_PAGE.DAT is read from the directory TRIGMON$SCALERS. This file contains the basic layout of the viewports (hereafter referred to as pages). The page layout is written to the viewports line by line using UIPACK routines. To adjust the basic page layout, it is necessary to adjust this file and the initialization routine.

LUMMON displays the page menu on receiving the first event. Choosing a page sets a logical for the event routine. There is one logical for each page – the one that is true is associated with the displayed page. At the end of the event routine, the page logicals are looked at and the proper display routine then called.

Each of these display routines exist as separate subroutines in the TRIGMON$SCALERS

area. They use UIPACK routines to write characters to particular locations in the viewport. After all the new values have been written, the viewport is updated.

B.2.3 Program Interpretation

All of the important calculations are done in the event routine SCLEVT. It takes the information from the various banks – SCLD, TAGC, TL2D – and calculates the rates, deadtimes, livetimes, cross sections, and correlations for quantities of interest. The routine has undergone a fair amount of change as the scalers and the scaler banks themselves changed (in terms of the gating, addition/subtraction of Level 0, and other changes). Tony and I tried to document what we were doing inside the code, so most of it can be understood by reading the comments. In addition, consult trigger note ?? for information describing the scaler channels.

B.3 Trigger Names Database

B.3.1 Introduction

The trigger names database was created to give the trigger group some control over the creation of various triggers. It keeps the trigger names unique, up to a point. When a physics table is parsed, there are checks against triggers which have been used prior to this particular table. If a trigger name matches one in the database, then checks are made to make sure that the trigger conditions also match. If they don't match, then parsing is stopped and the table is not prepared for use. I do not check to see that the conditions (selects, parameters, cuts, and executes, etc.) are also unique.

B.3.2 A little more explanation of exactly what is done

There is a series of routines that are executed when a physics table is parsed, which, in essence, re-parse the physics table. It creates a format which, I hope, is transparent to changes in the trigger definition (e.g., switching the order of selects, executes, etc., or writing 1.0 rather than 1.) which do not change the required criteria. The triggers in this format are what are placed into the database. For trigger in the physics table, the trigger name and level are compared against what is already in the database.

If a match is found, the conditions within the trigger are checked. If they match, then execution continues and the next trigger in the physics table is checked. If the conditions do not match, then the parsing is stopped. A printout of the trigger in the database and the trigger in the physics table is sent to the control room printer. The conditions must be made to match or the trigger name must be changed. One then must reparse the physics table.

If there is no current trigger in the database having the same name and level as the trigger of interest, then one may add this trigger to the database. If one does not want to add the trigger to the database, then parsing is stopped. We do not want to parse physics tables containing triggers which are not in the database. If one does want to add to the database, another decision must be made. Is the trigger going to be used for diagnostic purposes or for physics purposes? Triggers used to explore cross sections as a function of threshold should be entered as diagnostic triggers, since designating a trigger as a physics trigger assigns a TAGB bit to that particular trigger name. TAGB bits are used in the offline event selection routine TRGSEL and should be conserved whenever possible.

B.3.3 What to do if things go wrong

There exists a program, called DUMP_DB, which dumps to the terminal exactly what is in the trigger name database. Run this program, invoked by the symbol "DUMP_DB", and look at what is in the database. It shows the summary, by trigger number, level number, TAGB number, and trigger name, of all the triggers entered. After displaying the summary, it asks for which trigger one would like to dump. The trigger number is the key to use here. The triggers are entered in chronological order, so the last entry to the database is the most recent one.

If the error message from the parser concerns the status of the database itself, e.g. "Unable to open ", one can check to see who is accessing the cdfdb by issuing the dcl command "SHOW DEV/FILE CALIB_DSK2". It will show exactly who is accessing the cdfdb. The files which concern the trigger database are in the directory [cdfdb.production.trigtabl.prm]. Only one program can have the database open with WRITE access (as the parser does), so anyone else using the trigger database can cause problems. This situation also means that one can only parse one physics table at a time (until the database checking is complete - then one can begin parsing a second table).

Issuing a Cntl Y during the database checking part of the program will stop the parser, but it will also leave the database in a bad state. If the program appears hung up, check to see if the database is opened for access (by using the show dev/file calib_dsk2 command on the cpu the program is running on). If it is still opened for access the parser, DON'T use Cntl Y!!!!! If the database is not opened for access, it may be ok but don't count on it. Using Cntl Y during database sessions can seriously disrupt the database structure and should only be done if absolutely necessary.

I keep a file in the area TRIGGER$WORK_P called trigger.names which contains a somewhat up to date summary of the trigger database. If the database gets screwed up, it is what I use to for restoration purposes. The program BADNEWS in the

same area creates the file, so if the database does get screwed up, try to run this program and check what comes out. It should be the same as Dump_Db.

B.3.4 Details about the program execution

Each trigger is read in from the physics table and manipulated, using UIPACK, into a unique format. This formatting is done in two steps. First, the trigger is read in and SELECTS, EXECUTES, CUTS, PARAMETERS, etc. are picked off. There is no checking of syntax here - syntax checking is done in a different routine of the parsing code. Once all these keywords are found, they are then arranged into the format for checking against the database.

The routine TRIGGER_DB takes the physics table, finds the level, and then looks for the keyword TRIGGER. After finding this keyword, it does a line by line checking for SELECT, EXECUTE, PREREQUISITE, PARAMETER, CUT, CONSTRAINT, FRACTION, or TRIGGER. All of these, except CONSTRAINT and TRIGGER, are used as flags to build lines in the format. Hardware constraints are not kept in the database and when the trigger keyword is found (for the second time), the program branches and does the database checking. The rest of the line is then read in, on a word by word basis.

Character arrays, which contain the various lines from the physics table, are constructed for each type of keyword. I also keep count of the number of EXECUTES, SELECTS, etc., and the associated CUTs/PARAMETERs for each of these. These arrays are then passed to a second routine, which builds the trigger into the proper format.

The routine BUILD_COMPARE is responsible for this procedure. It takes these arrays and alphabetizes them. After alphabetizing these arrays themselves, which gets a little hairy because I have arrays of pointers to handle as well, they are placed into another character array. The ordering now looks like this:

TRIGGER trigger_name

LEVEL #

EXECUTE A.....

PARAMETER C....

EXECUTE B.....

PARAMETER A....

SELECT L....

CUT H....

CUT O....

END_TRIGGER

Here are several samples from the database:

```
TRIGGER          STIFF_TRACK
LEVEL            2
SELECT           STIFF_CLUSTER
CUT               NUMBER_OF_STIFF_CLUSTERS          >=          2.00
END TRIGGER

TRIGGER          STIFF_TRACK_2PT5
LEVEL            3
SELECT           PTHARD
PARAMETER         TALK_TO
NUMBER_TRACKS       2.000000
PT_CUT              2.500000
END_TALK
END TRIGGER
```

It all works well, except for the Level 3 talk_to's. The Level 3 talk_to's did not have a strict syntax requirement, so they sometimes get confusing to parse. What I ended up doing is alphabetizing all lines in between the PARAMETER TALK_TO and the END_TALK. Since UIPACK is used to read everything in, all comments are then lost. In the case above, the talk_to section was written using verbs and then cut values on the same line. In the following example, the talk_to section used button numbers and then a cut value on the next line — they were all commented but this aid got lost in the parsing.

```
TRIGGER          PHOTON_GAS_4_PEM
```

```
LEVEL           3
EXECUTE         CALORIMETRY
EXECUTE         EMCLST
EXECUTE         FHA_CABLE
EXECUTE         FILT_GAS
EXECUTE         NCABLE
PREREQUISITE    PHOTON_GAS_10
SELECT          L3PHO
PARAMETER        TALK_TO
-1
.7
0
1
10
11
13
2
7.5
8
85
9
999.
999.
999.
999.
END_TALK
END TRIGGER
```

This should be changed for the next run.

The trigger name is then checked against the database. The TGB component is used. This bank has a summary of trigger number (a counter), trigger level, TAGB bit number, and trigger name. Comparison is made first by trigger level and name. If there exists a trigger in the database with the same name, then the associated TRG component is fetched (using the trigger number as the database run number). A line by line comparison is then done. If everything agrees, then the program continues parsing the physics table. When things are different, an error is produced, the trigger in the database and the trigger in the physics table are

printed out, and the parser is exited without creating the necessary files for using the physics table.

When the trigger is new, then the option of entering it into the database is given to the user. If the user does not want to enter the trigger into the database, the parser is stopped (we don't want to run with triggers we don't know about). If everything is successful, the program will then continue on to the next trigger in the physics table.

B.3.5 Some gritty database details

The trigger names database is one database in the CDF database. Its name is 'TRIGTABL', type PRM, and it has one attribute, L12. There exist two components paired with this attribute, TRG and TGB. The TRG component contains the actual triggers, put into a unique text format for comparisons. The TGB component keeps a running summary of the triggers entered into the database, as well as the level for the trigger and the TAGB bit assigned to that particular trigger name. It keeps a pointer into the TRG component for every trigger.

Appendix C

The CDF Collaboration

1988-89

F. Abe,[8] D. Amidei,[4] G. Apollinari,[11] M. Atac,[4] P. Auchincloss,[14] A. R. Baden,[6] A. Bamberger,[19] A. Barbaro-Galtieri,[9] V. E. Barnes,[12] F. Bedeschi,[11] S. Behrends,[2] S. Belforte,[11] G. Bellettini,[11] J. Bellinger,[18] J. Bensinger,[2] A. Beretvas,[4] J. P. Berge,[4] S. Bertolucci,[5] S. Bhadra,[7] M. Binkley,[4] R. Blair,[1] C. Blocker,[2] A. W. Booth,[4] G. Brandenburg,[6] D. Brown,[6] E. Buckley,[14] A. Byon,[12] K. L. Byrum,[18] C. Campagnari,[3] M. Campbell,[3] R. Carey,[6] W. Carithers,[9] D. Carlsmith,[18] J. T. Carroll,[4] R. Cashmore,[19] F. Cervelli,[11] K. Chadwick,[4] G. Chiarelli,[5] W. Chinowsky,[9] S. Cihangir,[4] A. G. Clark,[4] D. Connor,[10] M. Contreras,[2] J. Cooper,[4] M. Cordelli,[5] D. Crane,[4] M. Curatolo,[5] C. Day,[4] S. Dell'Agnello,[11] M. Dell'Orso,[11] L. Demortier,[2] P. F. Derwent,[3] T. Devlin,[14] D. DiBitonto,[15] R. B. Drucker,[9] J. E. Elias,[4] R. Ely,[9] S. Errede,[7] B. Esposito,[5] B. Flaugher,[14] G. W. Foster,[4] M. Franklin,[6] J. Freeman,[4] H. Frisch,[3] Y. Fukui,[8] Y. Funayama,[16] A. F. Garfinkel,[12] A. Gauthier,[7] S. Geer,[6] P. Giannetti,[11] N. Giokaris,[13] P. Giromini,[5] L. Gladney,[10] M. Gold,[9] K. Goulianos,[13] H. Grassmann,[11] C. Grosso-Pilcher,[3] C. Haber,[9] S. R. Hahn,[4] R. Handler,[18] K. Hara,[16] R. M. Harris,[9] J. Hauser,[3] T. Hessing,[15] R. Hollebeek,[10] L. Holloway,[7] P. Hu,[14] B. Hubbard,[9] B. T. Huffman,[12] R. Hughes,[10] P. Hurst,[7] J. Huth,[4] M. Incagli,[11] T. Ino,[16] H. Iso,[16] H. Jensen,[4] C. P. Jessop,[6] R. P. Johnson,[4] U. Joshi,[4] R. W. Kadel,[4] T. Kamon,[15] S. Kanda,[16] D. A. Kardelis,[7] I. Karliner,[7] E. Kearns,[6] R. Kephart,[4] P. Kesten,[2] R. M. Keup,[7] H. Keutelian,[7] S. Kim,[16] L. Kirsch,[2] K. Kondo,[16] S. E. Kuhlmann,[1] E. Kuns,[14] A. T. Laasanen,[12] J. I. Lamoureux,[18] W. Li,[1] T. M. Liss,[7] N. Lockyer,[10] C. B. Luchini,[7] P. Maas,[4] M. Mangano[11] J. P. Marriner,[4] R. Markeloff,[18] L. A. Markosky,[18] R. Mattingly,[2] P. McIntyre,[15] A. Menzione,[11] T. Meyer,[15] S. Mikamo,[8] M. Miller,[3] T. Mimashi,[16] S. Miscetti,[5] M. Mishina,[8] S. Miyashita,[16] Y. Morita,[16] S. Moulding,[2] A. Mukherjee,[4] L. F. Nakae,[2] I. Nakano,[16] C. Nelson,[4] C. Newman-Holmes,[4] J. S. T. Ng,[6] M. Ninomiya,[16] L. Nodulman,[1] S. Ogawa,[16] R. Paoletti,[11] A. Para,[4] E. Pare,[6] J. Patrick,[4] T. J. Phillips,[6] R. Plunkett,[4] L. Pondrom,[18] J. Proudfoot,[1] G. Punzi,[11] D. Quarrie,[4] K. Ragan,[10] G. Redlinger,[3] J. Rhoades,[18] M. Roach,[17] F. Rimondi,[19] L. Ristori,[11] T. Rohaly,[10] A. Roodman,[3] A. Sansoni,[5] R. D. Sard,[7] A. Savoy-Navarro,[4] V. Scarpine,[7] P. Schlabach,[7] E. E. Schmidt,[4] M. H. Schub,[12] R. Schwitters,[6] A. Scribano,[11] S. Segler,[4] Y. Seiya,[16] M. Sekiguchi,[16] P. Sestini,[11] M. Shapiro,[6] M. Sheaff,[18] M. Shochet,[3] J. Siegrist,[9] P. Sinervo,[10] J. Skarha,[18] K. Sliwa,[17] D. A. Smith,[11] F. D. Snider,[3] R. St. Denis,[6] A. Stefanini,[11] R. L. Swartz, Jr.,[7] M. Takano,[16] K. Takikawa,[16] S. Tarem,[2] D. Theriot,[4]

M. Timko,[15] P. Tipton,[9] S. Tkaczyk,[4] A. Tollestrup,[4] G. Tonelli,[11] J. Tonnison,[12] W. Trischuk,[6] Y. Tsay,[3] F. Ukegawa,[16] D. Underwood,[1] R. Vidal,[4] R. G. Wagner,[1] R. L. Wagner,[4] J. Walsh,[10] T. Watts,[14] R. Webb,[15] C. Wendt,[18] W. C. Wester, III,[9] T. Westhusing,[11] S. N. White,[13] A. B. Wicklund,[1] H. H. Williams,[10] B. L. Winer,[9] A. Yagil,[4] A. Yamashita,[16] K. Yasuoka,[16] G. P. Yeh,[4] J. Yoh,[4] M. Yokoyama,[16] J. C. Yun,[4] F. Zetti[11]

[1] *Argonne National Laboratory, Argonne, Illinois 60439*

[2] *Brandeis University, Waltham, Massachusetts 02254*

[3] *University of Chicago, Chicago, Illinois 60637*

[4] *Fermi National Accelerator Laboratory, Batavia, Illinois 60510*

[5] *Laboratori Nazionali di Frascati, Istituto Nazionale di Fisica Nucleare, Frascati, Italy*

[6] *Harvard University, Cambridge, Massachusetts 02138*

[7] *University of Illinois, Urbana, Illinois 61801*

[8] *National Laboratory for High Energy Physics (KEK), Tsukuba, Ibaraki 305, Japan*

[9] *Lawrence Berkeley Laboratory, Berkeley, California 94720*

[10] *University of Pennsylvania, Philadelphia, Pennsylvania 19104*

[11] *Istituto Nazionale di Fisica Nucleare, University and Scuola Normale Superiore of Pisa, I-56100 Pisa, Italy*

[12] *Purdue University, West Lafayette, Indiana 47907*

[13] *Rockefeller University, New York, New York 10021*

[14] *Rutgers University, Piscataway, New Jersey 08854*

[15] *Texas A&M University, College Station, Texas 77843*

[16] *University of Tsukuba, Tsukuba, Ibaraki 305, Japan*

[17] *Tufts University, Medford, Massachusetts 02155*

[18] *University of Wisconsin, Madison, Wisconsin 53706*

[19] *Visitor*

References

[1] O. Klein, in *Les Nouvelles Théories de la Physique*, Proceedings of a symposium held in Warsaw, 30 May - 3 June 1938 (Institut International de Cooperation Intellectuelle, Paris, 1938) p. 6.

[2] See P. Hung and C. Quigg, Science **210**, 1205 (1980) for an excellent historical review of the evolution of the intermediate vector boson hypothesis.

[3] E. Fermi, Ric. Sci., **4**, 491 (1933); reprinted in E. Fermi, *Collected Papers*, E. Segré, et al., editors (Univ. of Chicago Press, Chicago, 1962) vol. 1, pp. 538–544 and Z. Phys. **88**, 161 (1934).

[4] J. Schwinger, Phys. Rev. **73**, 416 (1948); S. Tomonaga, Phys. Rev. **74**, 224 (1948); R.P. Feynman, Phys. Rev. **74**, 939 (1948).

[5] C.N. Yang and R.L. Mills, Phys. Rev. **96**, 191 (1954).

[6] J. Schwinger, Ann. Phys. **2**, 407 (1957).

[7] Y. Nambu, Phys. Rev. Lett. **4**, 380 (1960).

[8] J. Goldstone, Nuovo Cim. **19**, 154 (1961).

[9] P.W. Higgs, Phys. Rev. Lett. **13**, 508 (1964); Phys. Rev. **145**, 1156 (1966).

[10] S.L. Glashow, Nucl. Phys. **22**, 579 (1961); S. Weinberg, Phys. Rev. Lett. **19**, 1264 (1967); A. Salam, in *Elementary Particle Physics*, ed. by N. Svartholm (Almqvist and Wiksells, Stockholm, 1968), p. 367.

[11] G. Arnison, et al., Phys. Lett. **122B (1983)** 103; Phys. Lett. **126B** (1983) 398; Phys. Lett. **129B** (1983) 273; Phys. Lett. **134B** (1983) 469; M. Banner, et al., Phys. Lett. **122B** (1983) 476; P. Bagnaia, et al., Phys. Lett. **129B** (1983) 130.

[12] R. Burns, et al., Phys. Rev. Lett. **15**, 830 (1965); R. Lamb, et al., Phys. Rev. Lett. **15**, 800 (1965); P.J. Wanderer, et al., Phys. Rev. Lett. **23**, 729 (1969).

[13] G. 't Hooft, Nucl. Phys. **B33**, 173 (1971); **B35**, 167 (1971).

[14] B. Hasert, et al., Phys. Lett. **B46**, 138 (1973); A. Benvenuti, et al., Phys. Rev. Lett. **32**, 800 (1973).

[15] C. Rubbia, P. McIntyre, and D. Cline, in Proc. Int. Neutrino Conf. Aachen, 1976, (Vieweg, Braunshweig, 1977).

[16] P. Jenni, in Proceedings of the 1987 International Symposium on Lepton and Photon Interactions at High Energies, Hamburg, Federal Republic of Germany, ed. by W. Bartel and R. Rückl (North Holland Physics Publishing Division, Amsterdam, 1988) p. 341.

[17] F. Abe, et al., Phys. Rev. Lett. **62**, 1005 (1989).

[18] F. Abe, et al., Phys. Rev. Lett. **64**, 157 (1990).

[19] Y. Yamaguchi, Il Nuovo Cimento **43A**, 193 (1966); S.D. Drell and T-M. Yan, Phys. Rev. Lett. **25**, 316 (1970).

[20] Descriptions of the Standard Model can be found in V.D. Barger and R.J.N. Phillips, *Collider Physics* (Addison-Wesley, Redwood City, Ca. 1987) pp.1–66 and C. Quigg, *Gauge Theories of the Strong, Weak, and Electromagnetic Interactions* (Benjamin/Cummings, Reading, Ma. 1983) pp. 106–118.

[21] See C. Quigg, *Gauge Theories of the Strong, Weak, and Electromagnetic Interactions* (Benjamin/Cummings, Reading, Ma. 1983) for a description of structure function parametrizations.

[22] G. Altarelli, et al., Nucl. Phys. **246B**, 12 (1984).

[23] F. Abe, et al., Nucl. Instr. and Meth. **A271** (1988) 387.

[24] The CDF coordinate system defines Z along the proton-beam direction, θ as the polar angle, and ϕ as the azimuthal angle. The pseudorapidity, η, is defined $\eta = -\ln(\tan(\frac{\theta}{2}))$

[25] L. Balka, et al., Nucl. Instr. and Meth. **A267** (1988) 272.

[26] F. Abe, et al., Phys. Rev. Lett. **63**, 720 (1989).

[27] S. Bertolucci, et al., Nucl. Instr. and Meth. **A267** (1988) 301.

[28] F. Abe, et al., Phys. Rev. Lett. **62**, 613 (1989).

[29] Y. Fukui, et al., Nucl. Instr. and Meth. **A267** (1988) 280.

[30] W. Carithers, et al., to be submitted to Nucl. Instr. and Meth.

[31] G. Brandenburg, et al., Nucl. Instr. and Meth. **A267** (1988) 257.

[32] S. Cihangir, et al., Nucl. Instr. and Meth. **A267** (1988) 249.

[33] F. Snider, et al., Nucl. Instr. and Meth. **A268** (1988) 75.

[34] F. Bedeschi, et al., Nucl. Instr. and Meth. **A268** (1988) 50.

[35] F. Abe, et al., to be submitted to Nucl. Instr. and Meth. (Aseet's paper on CTC alignment).

[36] D. Amidei, et al., Nucl. Instr. and Meth. **A269** (1988) 51.

[37] J.T. Carroll, et al., "The CDF Level 3 Trigger", to be submitted to Nucl. Instr. and Meth.

[38] G.W. Foster, et al., Nucl. Instr. and Meth. **A269** (1988) 93.

[39] M. Miller, Ph.D. Thesis, University of Pennsylvania, 1989 (unpublished).

[40] We do not use this E_T in our calculation of the isolation. We use the cluster E_T for this calculation, defined from the calorimeter position, the event vertex, and the beam direction.

[41] K. Yasuoka, et al., Nucl. Instr. and Meth. **A267** (1988) 315.

[42] R.G. Wagner (unpublished), based on calculations by F. Berends et al., Z. Phys. **C 27**, 155 (1985); F. Berends and R. Kleiss, Z. Phys. **C 27**, 365 (1985).

[43] F. Abe, et al., to be submitted to Phys. Rev. D.

[44] J. Proudfoot, for the Proceedings of the Workshop on Calorimetry for the Superconducting Supercollider, ANL-HEP-CP-89-40-mc (microfiche) March 1989.

[45] E. Kearns, Ph.D. Thesis, Harvard University, 1990 (unpublished).

[46] Note that this threshold is in tower energy, not tower transverse energy.

[47] A.D. Martin, R.G. Roberts, and W.J. Stirling, Mod. Phys. Lett. A **4**, 1135 (1989).

[48] D. Duke and J. Owens, Phys. Rev. D **30**, 49 (1984).

[49] E. Eichten, I. Hinchliffe, K. Lane, and C. Quigg, Rev. Mod. Phys. **56**, 579, (1984).

[50] F. Paige and S.D. Protopopescu, ISAJET Monte Carlo Version 6.21, BNL Report No. BNL38034, 1986 (unpublished).

[51] Ian Hinchliffe (private communication). We used Version 3.08.

[52] U. Amaldi, et al., Phys. Rev. D **36**, 1385 (1987).

[53] The transverse mass is defined to be $\sqrt{E_T \not{E}_T(1-\cos\alpha)}$, where α is the azimuthal angle between the electron E_T and $\not{E}_T$.

[54] F. Abe, et al., to be submitted to Phys. Rev. D.

[55] F. Abe, et al., Phys. Rev. Lett. **62**, 613, (1989).

[56] If the event fractions (corrected for efficiencies) seen in data are used rather than the expected fractions, the value for ϵ_Z is 0.81 ± 0.05, where the increase in the uncertainty comes from the limited statistics of the data sample.

[57] K. Sliwa, in Proceedings of the 25th Moriond Conference, Hadronic Session, Les Arcs, France, March 1990 (to be published).

[58] G. Altarelli, et al., Nucl. Phys. **B308** 724 (1988).

[59] M. Bozzo, et al., Phys. Lett. **147B** 329 (1984).

[60] J. Gannon, et al., "Flying Wires at Fermilab", Proc. 1989 IEEE Part. Acc. Conf., Chicago (1989), p.1513.

[61] C.D. Moore, et al., "Single Bunch Intensity Monitoring System using an Improved Wall Current Monitor", Proc. 1989 IEEE Part. Acc. Conf., Chicago (1989), p. 68.

[62] N. Gelfand, private communication.

[63] We wish to thank the Fermilab Accelerator Division, especially N. Gelfand, for the help in understanding the accelerator data.

[64] D. Johnson, Fermilab Technical Memo TM-1554, Jan. 1989.

[65] We have taken f_{DA} from Table 1 of reference [59] and interpret it as the fraction of the total inelastic cross section seen in the UA4 trigger counters.

[66] We have used $\frac{\sigma_{el}}{\sigma_{tot}} = 0.215$, $\sigma_{tot} = 59.5 \pm 1.4 \pm 1.2$ mb, and $f_{DA} = 0.827$.

[67] S. Belforte, private communication.

[68] K. Ellis, in Proceedings of the Eighth Topical Workshop on Proton-Antiproton Physics, Castiglione, Italy, September 1989 (to be published).

[69] J. Alitti, et al., CERN-EP/90-20, Feb. 1990, submitted to Z. Phys. C.

[70] J. Alitti, et al., CERN-EP/90-22, Feb. 1990, submitted to Phys. Lett. B.

[71] F. Halzen and M. Mursula, Phys. Rev. Lett. **51**, 857 (1983); K. Hikasa, Phys. Rev. D **29**, 1939; N.G. Deshpande et al., Phys. Rev. Lett. **54**, 1757 (1985); A.D. Martin, R.G. Roberts, and W.J. Stirling, Phys. Lett. **189B**, 220 (1987); E.L. Berger, F. Halzen, C.S. Kim, and S. Willenbrock, Phys. Rev. D **40**, 83 (1989).

[72] A.D. Martin, W.J. Stirling, and R.G. Roberts, Phys. Lett. **228B**, 149 (1989).

[73] F. Dydak, in Proceedings of the 25th International Conference on High Energy Physics, Singapore, August 1990 (to be published).

[74] We use $\Gamma(Z^0 \rightarrow e^+e^-) = 82.8 \pm 0.6$ MeV; see W.F.L. Hollik, DESY Report No. 88-188, 1988 (unpublished).

[75] We used the method of the Particle Data Group, M. Aguilar, et al., Phys. Lett. **204B**, (1988), for extracting limits in the case of bounded physical regions.